**ORIGINAL PAPER**

# Exhumation dynamics of high-pressure metamorphic rocks from the Voltri Unit, Western Alps: constraints from phengite Rb–Sr geochronology

Andrew J. Smye[1] · Spencer M. Seman[1] · Marco Scambelluri[2] · Paul G. Starr[3] · Laura Federico[2]

## Abstract

The Voltri Unit and adjacent Tertiary Piedmont Basin, Western Alps, preserve complementary bedrock and sedimentary archives of Alpine subduction and exhumation. Combined *PT* modeling and phengite Rb–Sr geochronology of bedrock and clast samples shows that Fe–Ti metagabbros and metasediments preserve a record of protracted high-pressure metamorphism, between ~ 50 and ~ 40 Ma. Bedrock and clast Fe–Ti metagabbros yield similar eclogite-facies peak conditions, between 23 and 25 kbar, 510–530 °C; phengite, zoned in celadonite content, with cores > 3.5 Si c.p.f.u. and rims < 3.3 Si c.p.f.u., constrains the timing of exhumation between 24 and 20 kbar to 45–49 Ma. A single impure quartzite bedrock sample records peak-*P* conditions of 18–19 kbar, 450–470 °C; partial phengite equilibration in this sample occurred continuously between 19 and 12 kbar, between ~ 45 and ~ 40 Ma. Exhumation-related recrystallization of high-pressure phengite to low-Si phengite in two metasedimentary samples occurred between ~ 33 and ~ 30 Ma, contemporaneous with the onset of deposition in the Tertiary Piedmont Basin and consistent with previous ${}^{40}Ar–{}^{39}Ar$ constraints on the timing of greenschist metamorphism. Combined with existing ages from the ophiolite, these data show that peak subduction-related high-pressure conditions, between ~ 18 and ~ 25 kbar, were attained at different times across the Voltri Unit, between ~ 50 and ~ 40 Ma, implying that the Voltri Unit comprises an assembly of discrete lithotectonic units that were juxtaposed prior to erosion and deposition in the Tertiary Piedmont molasse basin. The *PTt* data reported here support a model in which individual sheets of high-pressure material were detached from the downgoing plate, partially exhumed from peak pressures to blueschist facies conditions, while subduction continued, and were stored for > 10 Myr until subduction ceased on arrival of the European continent into the orogenic wedge. As shear tractions on the plate interface are considered to exceed available buoyancy forces for exhumation, we suggest that syn-subduction exhumation occurred along the wedge-plate interface.

✉ Andrew J. Smye
  smye@psu.edu

[1] Department of Geosciences, Penn State, University Park, PA 16803, USA

[2] Università degli Studi di Genova, UNIGE, Genova, Italy

[3] Department of Earth and Environmental Sciences, Boston College, Chestnut Hill, Boston, MA 02467, USA

## Introduction

High-pressure (*HP*) metamorphic rocks are the only direct probes of the physical and chemical conditions deep within subduction zones. However, they are anomalous in that they have been returned to the Earth's surface unlike the majority of subducted oceanic lithosphere. To accurately interpret the petrological information they record, it is, therefore, important to understand how *HP* metamorphic rocks are detached from the downgoing slab and returned to the Earth's surface.

Exhumation of *HP* metamorphic rocks requires either the removal of material that caused the high pressures, or tectonic transport of the *HP* rocks through the overlying subduction complex. Erosion likely controls the final stages of exhumation, but additional processes are required

for exhumation from mantle-depths (e.g., Platt 1993); these include corner flow (e.g., Cloos and Shreve 1988; Gerya, et al. 2002; Shreve and Cloos 1986), buoyancy-driven ascent of metasedimentary and serpentinite-rich bodies (e.g., England and Holland 1979; Hermann et al. 2000) and extension of the accretionary wedge (e.g., Jolivet et al. 2003). Analysis of Pressure–Temperature-time (*PTt*) data from *HP* metamorphic terranes shows that *HP* rocks are exhumed discontinuously, in short-lived episodes (< 15 Myr), during subduction of oceanic lithosphere (e.g., Agard et al. 2009,2018). These observations raise the questions: *does exhumation occur concurrently with active subduction, or, are accreted HP materials stored at depth while subduction continues?*

Retrograde *PTt* paths derived from petrological investigations of exhumed *HP* terranes are considered to be accurate indicators of the timing of exhumation relative to subduction (Ernst 1988). Concurrent exhumation and subduction is expected to result in similar prograde and retrograde *PTt* paths due to continued underplating of cold oceanic lithosphere; examples of such a *PT* evolution are the blocks and coherent terranes of the Eastern Franciscan belt (Banno et al. 2000; Kimura et al. 1996; Maruyama and Liou 1988) and the lawsonite metabasalts from the Sivrihisar Massif, Turkey (Davis and Whitney 2006). In contrast, exhumation following the cessation, or pronounced deceleration of subduction, occurs through relaxing isotherms and is expected to result in near-isothermal retrograde *PTt* paths, as preserved by the Saih Hatat eclogite blocks, Oman (Warren and Waters 2006), Eastern Alpine blueschists and eclogites (Smye et al. 2011) and the Nevado-Filábride Complex, southern Spain (Sánchez-Vizcaíno et al. 2001).

This paper presents the results of a petrochronological investigation into the *PTt* evolution of blueschist- and eclogite-facies ophiolitic mafic rocks and metasediments of the Voltri *HP* Unit, Western Alps. Zoned phengite grains in a suite of *HP* samples record discrete intervals of *PTt* information that, collectively, constrain the tectonic history from Alpine subduction to exhumation and erosion. Constraints from phengite Rb–Sr geochronology and metamorphic phase equilibria show that eclogites and metasediments: (1) underwent *HP* metamorphism at depths between 60 and 80 km, (2) were partially exhumed, accreted and stored within the Alpine orogenic wedge for > 10 Myr, and (3) were finally exhumed following the cessation of subduction. These findings demonstrate the potential importance of storage of slab-top materials under forearc conditions for understanding subduction zone mass transfer.

## The Voltri Unit

The Voltri Unit is a dismembered metaophiolite suite, representing the remnants of the Alpine-Tethys oceanic realm located between the southernmost sector of the Western Alps and the northernmost sector of the Apennines. Subduction and exhumation occurred during convergence between the continental Europe and Adria (a promontory of the African continent) plates throughout the Cretaceous-Tertiary period (Polino et al. 1990; Vanossi et al. 1984). After Capponi et al. (2016), the Voltri Unit (Fig. 1) comprises: (1) high-pressure calcareous metasediments and metavolcanics (the Voltri-Rossiglione Unit
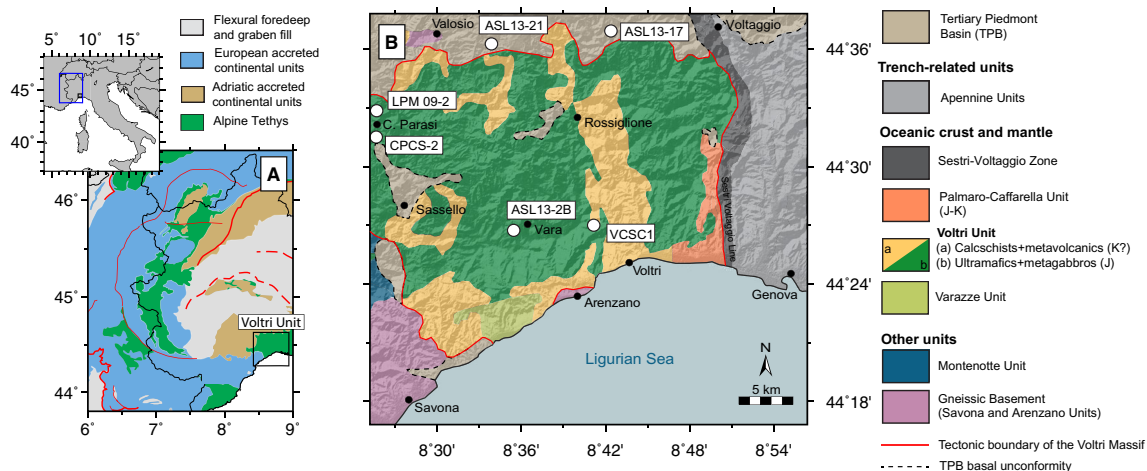


**Fig. 1** Tectonic context of the Voltri Unit. Panel **a**: major tectonic units of the Alpine chain after Schmid et al. (2004,2008); thick red lines represent deformation fronts (solid for exposed, dashed for subsurface) and thin red lines represent major Neogene faults. Box corresponds to region of interest shown in **b** Panel **b**: simplified geological map of the Voltri Massif superimposed on topographic relief. Units and tectonic boundaries are from Capponi et al., (2016); white text boxes refer to locations of samples used in this study. Note that the Voltri-Rossiglione Unit of previous workers corresponds to Voltri Unit of this map; similarly, the Beigua and Erro Tobbio Units are included in Voltri Unit

*Auct.*) associated with high-pressure serpentinites hosting eclogites, metarodingites, metagabbros and metabasalts (the Beigua Unit *Auct.*), and (2) variably-serpentinized oceanic mantle peridotite (the Erro-Tobbio Unit *Auct.*) that underwent Alpine subduction and eclogitization (Scambelluri et al. 1995). Combined, all these lithologies are interpreted to represent portions of the sedimentary cover, crust and mantle lithosphere of subducted and subsequently exhumed Tethyan oceanic lithosphere.

The Voltri Unit is overlain to the north by the Tertiary Piedmont basin that contains molasse deposits with Oligo-Miocene stratigraphic ages (Gelati et al. 1998; Lorenz 1969), including blueschist and eclogite clasts in the basal units. These clasts have been interpreted to derive from the Voltri Unit during denudation of pre-existing Alpine topography (e.g., Federico et al. 2005). To the west, the Unit is juxtaposed against Hercynian basement (the Savona and Arenzano Units), and to the east the high-pressure ophiolitic sequence of the Palmaro-Caffarella Unit (blueschist-facies) and of the Sestri-Voltaggio Zone (pumpellyite-actinolite facies) separates the Voltri Unit from the low-grade flysch of the Northern Apennines.

Bedrock eclogites in the central portion of the Voltri Unit (Vara region, Fig. 1) outcrop as meter-to-decameter-scale pods in a metamorphosed serpentinite matrix. On the basis of major element and REE compositions, the eclogites are similar to modern-day Fe–Ti gabbros (Morten, et al. 1979). Textural characteristics have been used to define two groups of eclogites: (1) massive eclogites containing coarse-grained sodic clinopyroxene rimmed by fine-grained coronas of garnet and rutile; and (ii) foliated eclogites with euhedral garnet embedded in a fine-grained matrix of glaucophane, omphacite and rutile.

Petrologic investigations have shown that the Voltri eclogites experienced peak metamorphic conditions of 18–25 kbar and 450 °C–550 °C, followed by a polyphase retrograde evolution through the blueschist, amphibolite, and greenschist facies (Brouwer et al. 2002; Cimmino and Messiga 1979; Ernst 1981; Federico et al. 2007a, b; Liou et al. 1998; Messiga 1987; Messiga and Scambelluri 1991; Messiga et al. 1995; Starr et al. 2020; Vignaroli et al. 2005). Of particular note is the uniformity of recent estimates of peak ecogite-facies conditions, ~ 500–525 °C and 23–25 kbar, recorded by Fe–Ti metagabbros across the Voltri Unit (Starr et al. 2020). Similar peak conditions have been documented in eclogite-facies lherzolites of the Erro-Tobbio Unit *Auct.* (Scambelluri et al. 1991), whereas *PT* constraints from the Voltri metasediments are loosely constrained due to pervasive, exhumation-related retrogression. Polyphase retrogression during decompression is evidenced by the occurrence of chloritoid, albite, chlorite, titanite and lower-Si phengite assemblages (e.g., Cimmino and Messiga 1979; Federico et al. 2005).

The tectonic evolution of the Voltri Unit is constrained by a variety of geochronological constraints derived from multiple radiogenic decay systems and from samples pertaining to both bedrock of the Voltri Unit and clasts of the adjacent Tertiary Piedmont Basin (TPB). Combined, these data constrain the timing of peak eclogite-facies conditions across the Voltri Unit to ~ 50–38 Ma. Using bulk garnet Sm–Nd geochronology, Starr et al. (2020) showed that *HP* conditions were first attained in the northwestern portion of the Voltri Unit at ~ 50 Ma, followed by peak metamorphism in the Voltri metasediments around ~ 47–44 Ma, and ~ 41–38 Ma in Fe–Ti metagabbros in the central portion of the Voltri Unit. These direct constraints on the timing of eclogite-facies metamorphism are supported by $^{40}Ar$–$^{39}Ar$ ages of zoned high-Si phengite, interpreted by Federico et al., (2005) to represent peak *HP* conditions at ~ 49 Ma, followed by blueschist and greenschist retrogression at 43–40 and 33 Ma, respectively. Phengite $^{40}Ar$–$^{39}Ar$ dates obtained from eclogite blocks from the Cascine Parasi Mélange unit are consistent with younger attainment of the eclogite-facies peak at ~ 43 Ma, followed by blueschist facies retrogression at 43–40 Ma. However, these dates are difficult to reconcile with a U–Pb (SHRIMP) baddeleyite age of 33.6 ± 1.0 Ma, interpreted to record the timing of eclogite-facies metamorphism in Ti-clinohumite-bearing, altered Fe–Ti gabbros of the Beigua Unit (Rubatto and Scambelluri 2003).

The stratigraphy of the TPB provides additional constraints on the tectonic evolution of the Voltri Massif. Basal horizons, characterized by continental-to-transitional and shallow marine sediments of the Molare Formation, have an Early Oligocene age of deposition (Blow 1969; Gelati and Gnaccolini 1982; Turco et al. 1994) and contain detrital phengite grains that yield two clusters of $^{40}Ar$–$^{39}Ar$ dates (Barbieri et al. 2003; Carrapa et al. 2003). The oldest population comprises dates of ~ 45–48 Ma that overlaps the timing of peak *HP* metamorphism preserved in bedrock units, whereas the younger population is defined by dates of ~ 32–34 Ma, spanning the first depositional stage of the TPB. Apatite (U-Th)/He and fission track thermochronology dates derived from both Oligo-Miocene deposits and the Voltri Unit, demonstrate that the basin was exhumed above 4 km by ~26 Ma (Vignaroli et al. 2010). Combined, these highly dispersed data demonstrate that the age and duration of *HP* conditions, and rates of subsequent exhumation are spatially variable across the Voltri Unit.

## Sample petrography

Samples in this study comprise white mica-bearing eclogites and metasediments collected from bedrock (LPM 09-2, ASL13-2B, VCSC1 and CPSC-2) and basal conglomerates of the TPB (ASL13-17 and ASL13-21). Sample locations are shown in Fig. 1, petrographic characteristics are discussed

and representative photomicrographs are presented in Fig. 2. In the text beneath, we refer to phengite as the solid solution series between muscovite, aluminoceladonite and celadonite (Rieder et al. 1998); all mineral abbreviations are after Whitney and Evans (2010).

## Bedrock samples

Sample LPM 09-2 is a mafic eclogite sampled from a meter-scale block in the northwestern sector of the Voltri Unit, along the Erro River, ca. 10 km north of Sassello (Fig. 1; La Pesca locality described by Scambelluri et al. 2016; 44° 33′ 23.15″ N; 8° 26′ 47.22″ E). It contains garnet, glaucophane, omphacite, phengite, rutile, epidote and quartz. Garnet forms mm-scale poikiloblasts with inclusion-rich cores and is wrapped by a penetrative foliation defined by blue amphibole and omphacite; epidote, rutile, quartz and blue amphibole are common as included phases. Multiphase mineral inclusions within the garnet cores consist of block-shaped aggregates of epidote, plagioclase and paragonite that are interpreted to derive from breakdown of former lawsonite. Idiomorphic phengite displays sharp grain boundaries and equilibrium microtextures with cogenetic garnet, omphacite and Na-rich amphibole (Fig. 2a). This sample was collected from the same location as Fe–Ti metagabbro V18-S617C01 reported by Starr et al. (2020).

Sample VCSC1 is a variably-retrogressed micaschist sampled from the central Voltri Unit (44° 28′ 34.48″ N; 8° 42′ 41.58″ E). It contains quartz, white-mica and plagioclase as major phases and carbonate, rutile, chlorite and tourmaline as accessory phases. Two generations of phengite are observed; one predates the penetrative foliation, whereas the other generation cross-cuts microlithons of recrystallized quartz (Fig. 2b). In each case, mica grains are between 100 and 200 μm long.

Sample ASL13-2B (44° 28′ 13.2″ N; 8° 36′ 50.7″ E) is a strongly foliated quartz-mica schist collected from the Vara region of the central Voltri Unit. It contains syntectonic quartz, phengite, carbonate and minor rutile, tourmaline and graphite. Phengite flakes exhibit kink bands and, along with graphite seams, define an *S-C* fabric; individual mica grains range from 50 to 500 μm length. Quartz grains have undergone recrystallization, show undulose extinction and form aggregates that define microlithons (Fig. 2c).

Sample CPSC-2 (44° 32′ 35″ N, 8° 28′ 56″ E) is a quartz-mica schist collected from the Cascine Parasi mélange (Federico et al. 2007a) and contains quartz, phengite, Na-amphibole, rutile, titanite, allanite-epidote and minor garnet. Phengite wraps euhedral poikiloblasts of zoned Na-amphibole and epidote; garnet is present as small idioblasts (< 1 mm diameter) that occur both within the matrix and as inclusions within Na-amphibole (Fig. 2d).

## Clast samples from the Tertiary Piedmont Basin

Sample ASL13-17 is a retrogressed eclogite clast collected from the base of the TPB (44° 37′ 11″ N; 8° 43′ 30″ E) and contains, in order of decreasing abundance glaucophane, epidote, garnet, rutile, phengite and quartz (Fig. 2e). Garnet porphyroblasts are disaggregated and heavily retrogressed to chlorite. Straight grain boundaries between relict garnet and glaucophane blasts indicate that these two phases were a part of the peak assemblage. The conspicuous absence of omphacite implies post-peak retrogression that involved the consumption of clinopyroxene and (re-) equilibration of glaucophane and epidote on exhumation through blueschist facies conditions.

ASL13-21 is a calcschist clast sampled from the base of the TPB (44° 36′ 11″ N; 8° 36′ 15″ E). It is characterized by the high-variance mineral assemblage: phengite, quartz and carbonate; rutile, graphite, chlorite and tourmaline are each present as accessory phases. Phengite is present as flakes (200–500 μm length) that define a dominant foliation that wraps aggregates of quartz and carbonate. Clots of chlorite are interpreted to have formed from the retrogression of precursor garnet (Fig. 2f).

# Analytical techniques

## Whole-rock and mineral compositions

Major element compositions of rock-forming mineral phases were determined using a Cameca SX-5 electron microprobe at the Materials Characterization Laboratory, Penn State. The instrument is equipped with four wavelength-dispersive spectrometers; operating conditions comprised a 20 kV accelerating voltage and a 20 nA beam current. The spot size was 2 μm for all analyses and on-peak counting time was 20 s for all elements. Natural and synthetic oxides were used for calibration standards.

Bulk rock major element analysis of selected bedrock and clast samples were performed at the Department of Earth and Environmental Sciences, Franklin and Marshall College, utilizing a PANalytical 2404 X-ray fluorescence (XRF) spectrometer and the methods presented in Boyd and Mertzman (1987).

## White-mica Rb–Sr geochronology

Whole-rock samples were crushed using a roller mill and washed with deionized water to remove fine particles. After passing through a 1 mm sieve, a Frantz isodynamic separator was employed to concentrate mica, garnet, and other mineral fractions. An agate mill was then used to reduce
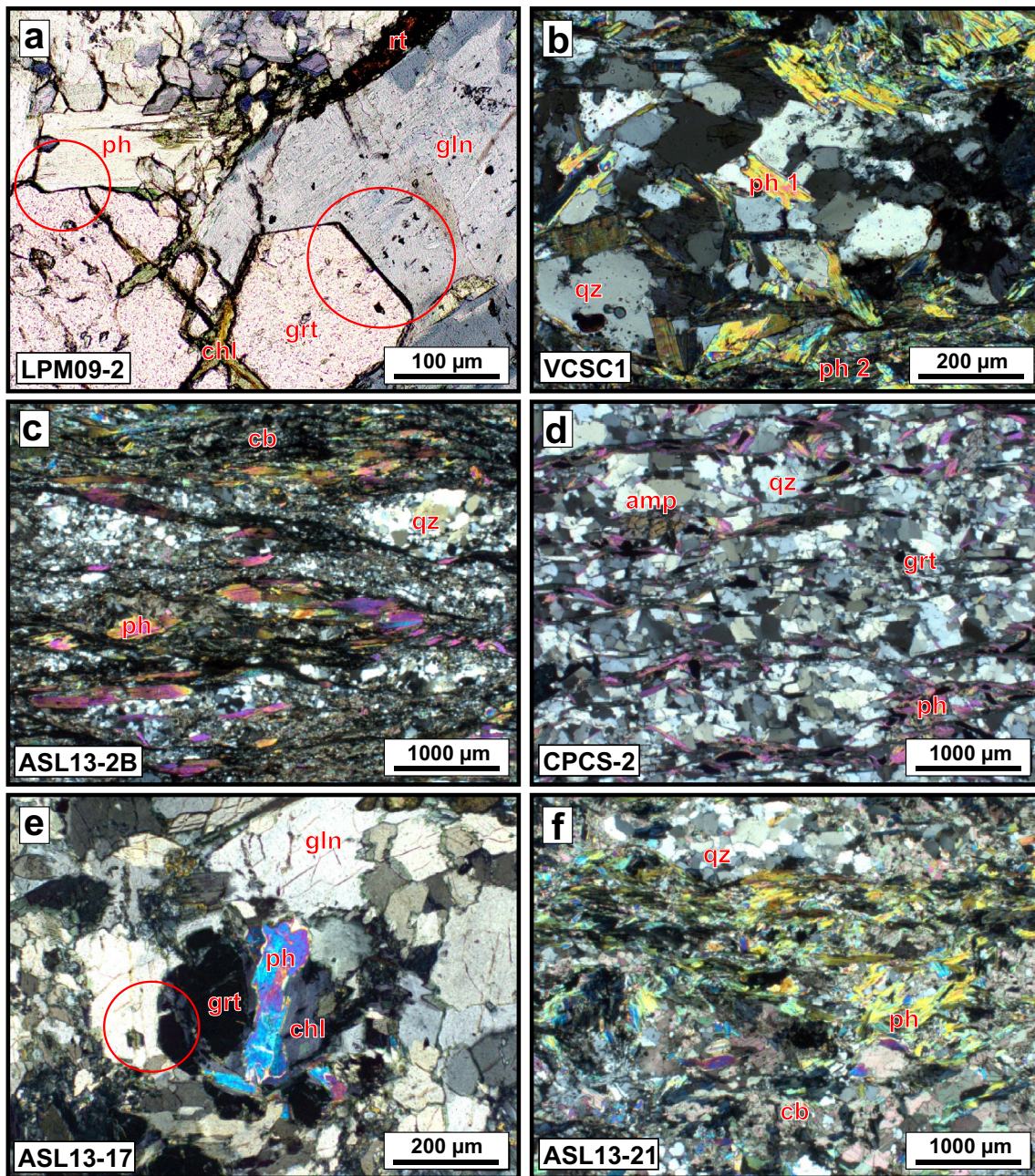
**Fig. 2** Sample petrography. Photomicrographs showing microtextural settings of white mica. Panel (**a**): close-up, plane polarized light (PPL) image of garnet, phengite and glaucophane in sample LPM 09-2. Red circles draw attention to straight grain boundaries between garnet and glaucophane (eastern red circle) and garnet and phengite (western) interpreted to represent textural equilibrium under peak *HP* conditions. Note the limited extent of retrograde chlorite growth at the expense of garnet. Panel (**b**): cross polarized light (XPL) image of phengite flakes in micaschist sample VCSC1. Abbreviations ph1 and ph2 refer to phengite generations that are aligned sub-parallel with and cross-cut the penetrative foliation, respectively. Panel (**c**): XPL image of penetratively deformed micaschist sample, ASL13-2B. Note the prominent *S-C* fabric defined by phengite flakes. Panel (**d**): XPL image of Na-amphibole- and garnet-bearing micaschist sample, CPCS-2. Phengite wraps idioblastic garnet and porphyroblasts of zoned Na-amphibole. Panel (**e**): XPL image of retrogressed mafic blueschist sample, ASL13-17. Garnet is disaggregated into chlorite and phengite. Straight grain boundaries between relict garnet and amphibole blasts (red circle) imply that these two phases were a part of the peak assemblage; note the absence of clinopyroxene. Panel (**f**): image (XPL) shows aggregates of phengite in calcschist sample ASL13-21. For all panels, mineral abbreviations are after Whitney & Evans (2010)

the mineral fraction size. Prior to digestion in a HF-HNO$_3$ solution, mineral fractions were spiked with a mixed $^{87}$Rb-$^{84}$Sr tracer. Spike isotope concentrations were calibrated using NISTSRM984, RbCl, and NISTSRM987, SrCO$_3$, gravimetric solutions and checked against the established Rb–Sr standard, NISTSRM607, K-Feldspar (Compston et al. 1969; Nebel and Mezger 2006). Following dissolution, Sr was isolated using the automated Prepfast-MC Sr-Ca separation method (Romaniello et al. 2015); the Prepfast-MC system was also utilized to separate Rb using a 2 mL column filled with AG50Wx8 resin. For samples, ASL13-21, and 17, both Sr and Rb were analyzed on a ThermoFisher Triton *Plus* TIMS at Pennsylvania State University. The Rb fractionation factor was determined by concurrent analysis of NISTSRM984 assuming an $^{87}$Rb/$^{85}$Rb$=0.3857$. All other Rb measurements were made using MC-ICP-MS (ThermoFisher Neptune, Metal Isotopes Laboratory, Penn State) and correcting for mass bias using concurrent analyses of Zr (Waight, et al. 2002). A nominal uncertainty of 1% (1σ) was assigned to $^{87}$Rb/$^{86}$Sr values based on the variability of NISTSRM607, measured concurrently. The instrument mean $^{87}$Sr/$^{86}$Sr for NISTSRM987 was $0.71025 \pm 0.00004$ between June 2017 and July 2018. An uncertainty of 0.01% was assigned to $^{87}$Sr/$^{86}$Sr determinations based on the propagated uncertainty of sample $^{87}$Rb/$^{86}$Sr, typically 0.05%. Isochron parameters were calculated using IsoplotR

(Vermeesch 2018) and the $^{87}$Rb decay constant of Nebel and Mezger (2011).

## Mineral chemistry

Major element compositions of white mica were collected for each sample that was dated by Rb–Sr geochronology; the compositions of other rock-forming minerals in samples LPM 09-2, ASL13-17 and CPCS-2 were also collected to support phase equilibria calculations. Mica, amphibole and garnet chemistry and compositional profiles are presented in Figs. 3, 4, 5, respectively. Representative mineral compositions are presented in Table 1.

Phengite is present in each of the samples; Si contents vary from 3.2 to 3.7 c.p.f.u. Mica grains in samples LPM 09-2, VCSC1, ASL13-2B and ASL13-21 are zoned in celadonite content with decreasing inverted tschermak substitution (MgSiAl$_{-2}$) from core to rim. Phengite cores generally exceed 3.4 c.p.f.u. Si, whereas rims are characterized by <3.3 c.p.f.u. Si (Fig. 3), implying that mica grains partially re-equilibrated during decompression. Paragonite is present as a minor alteration product around the rims of phengite grains in sample ASL13-17.

Zoned amphibole grains are present in samples LPM 09-2, ASL13-17 and CPCS-2. Microstructural evidence allows the distinction of three generations of amphibole in sample LPM
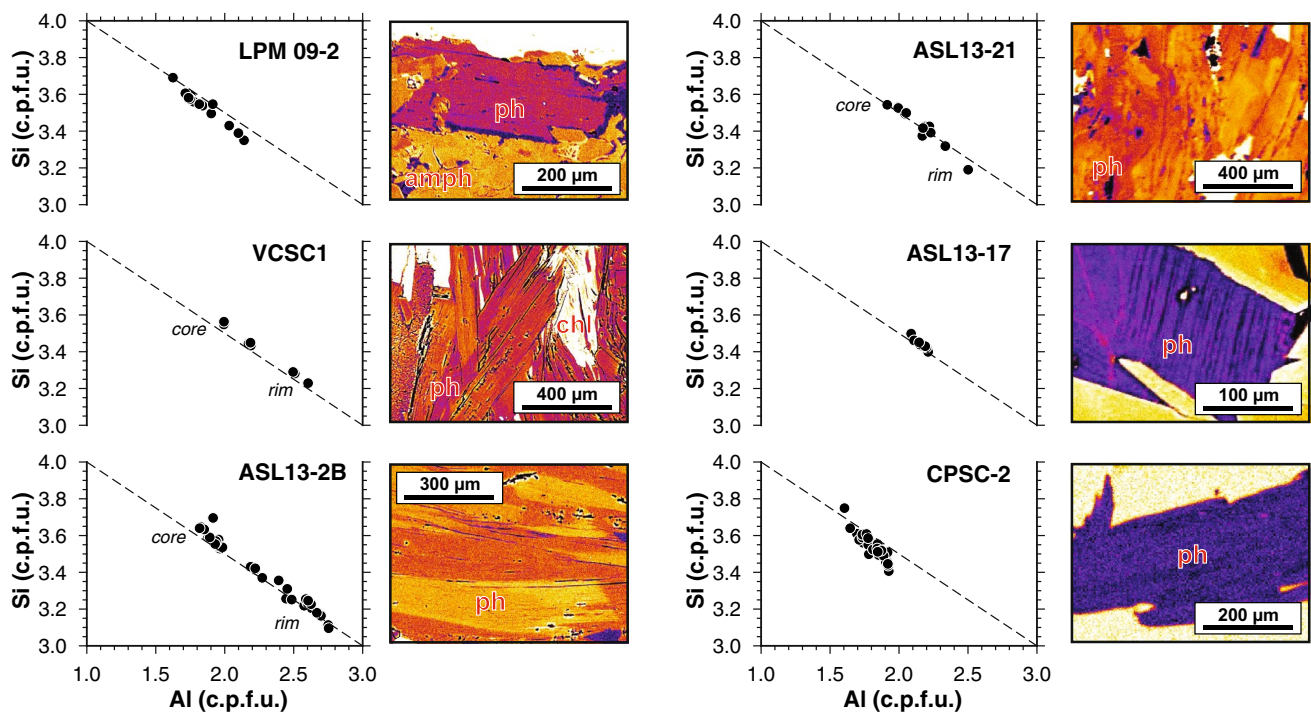


**Fig. 3** Mica chemistry. Figure shows Si against Al c.p.f.u. for white-mica from each of the samples investigated. Adjacent panels show false-color BSE images of individual mica grains. Note the pronounced zoning in average atomic number for VCSC1, ASL13-2 and ASL13-21
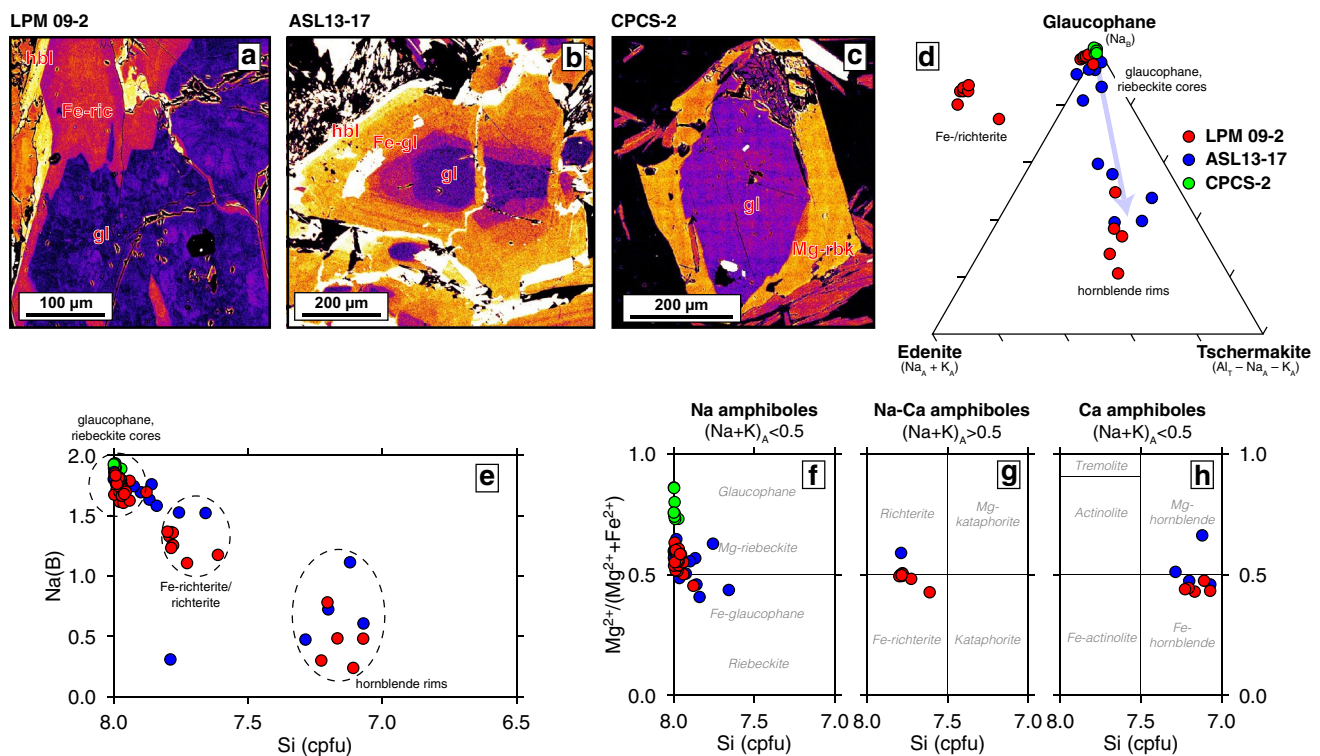
**Fig. 4** Na, Na–Ca and Ca amphibole chemistry. Panels **a**–**c** show modified BSE intensity images of zoned amphibole from samples LPM 09-2, ASL-17 and CPCS-2. Following Schumacher (2007), panel **d** expresses amphibole compositions in terms of the relative magnitudes of the three dominant amphibole substitution vectors: edenite ($Na_A$), glaucophane ($Na_B$) and tschermakite ($Al_T$-$Na_A$). Note that in this coordinate scheme, substitution along the richterite vector results in negative tschermakite values, as demonstrated by several analyses from LPM 09-2. Arrow marks the core-to-rim compositional vector from ASL13-17. Panel **e** shows $Na_B$ versus Si (c.p.f.u.) for all amphibole data. Panels **f**–**h** show classification diagrams for Na, Na–Ca and Ca amphiboles after Leake (1978), respectively. The color scheme for all plots is as shown in panel **d**

09-2: (1) mineral core domains of glaucophane-to-Mg-riebeckite composition ($Na_B > 1.5$, $(Na + K)_A < 0.5$, $X_{Mg} > 0.5$, where $X_{Mg} = Mg/(Mg + Fe^{2+})$) with minor substitution along edenite and tschermakite vectors (Fig. 4d); these regions exhibit patchy, irregular zonation in $X_{Mg}$ (values between 0.5 and 0.6; Fig. 4f), visible in BSE (Fig. 4a); (2) mantles of Fe-richterite-to-richerite ($Na_B = 1.0$–$1.5$, $(Na + K)_A > 0.5$, $X_{Mg}$ 0.4–0.5; Fig. 4g), and (3) narrow (< 50 μm), outermost rims composed of Fe-hornblende or barroisite ($Na_B < 1.0$, $(Na + K)_A < 0.5$, $X_{Mg}$ 0.4–0.5, Si 7–7.5 c.p.f.u.; Fig. 4h). Amphibole in sample ASL13-17 exhibits progressive zonation from Mg-riebeckite-to-glaucophane cores to Fe-glaucophane rims; several analyses of richterite were collected from growth zones proximal to glaucophane core domains. These zoned HP amphibole cores are overgrown by discrete, narrow rims (< 50 μm) of Fe- to Mg-hornblende composition (Fig. 4h). Finally, sample CPCS-2 exhibits two generations of Na amphibole: a central glaucophane core phase overgrown by euhedral rims of Mg-riebeckite (Fig. 4f). The main similarity in amphibole chemistry between each of the samples is the glaucophane-riebeckite cores, interpreted to represent high-pressure conditions. The two mafic samples,

LPM 09-2 and ASL13-17, exhibit similar magnitudes of retrograde tschermakite and edenite substitution in hornblende rim domains, consistent with formation during or following decompression from eclogite or blueschist facies conditions. However, it is worth noting that the continuous nature of the core-to-rim zonation observed in sample ASL13-17 is markedly different from the discrete overgrowths observed in sample LPM 09-2 and CPCS-2.

Zoned garnet is present in samples LPM 09-2, ASL13-17 and CPCS-2. Example chemical traverses and maps are presented in Fig. 5, and example chemical analyses are presented in Table 1. Garnet porphyroblasts in sample LPM 09-2 are almandine-rich solid solutions ($X_{alm} > 50$ molar %) and preserve at least two distinct growth zones (Fig. 5a, d). The internal zone dominates the volume of each garnet grain analyzed and is characterized by bell-shaped core-rim Mn zonation, implying prograde sequestration of elements according to Raleigh fractionation (yellow shading, Fig. 5d; core composition: $Alm_{55-67}Grs_{24-27}Prp_{24-27}Sps_{5-20}$). Chemical maps of Mn zonation reveal an external growth zone that spans the outermost ~ 100 μm radial distance and is characterized by low-Mn and Ca concentrations and an
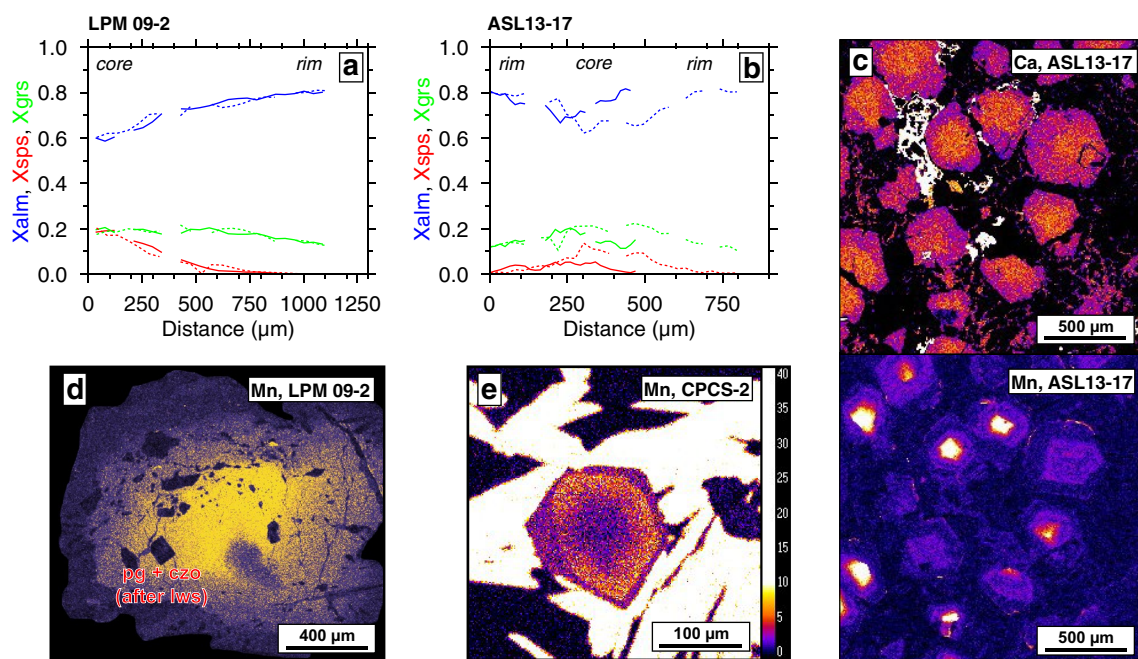
**Fig. 5** Garnet chemistry. Panels **a** and **b** show variation in mole fractions of almandine (blue), spessartine (red) and grossular (green) across individual garnet grains from samples LPM 09-2 and ASL13-17. Gaps in data correspond to inclusions; solid and dashed lines represent different traverses across different garnet crystals. Panel **c** shows Ca (upper) and Mn intensity maps for garnet from sample ASL13-17. Panel **d** shows Mn intensity in a garnet poikiloblast from sample LPM 09-2; note the pseudomorphs after lawsonite. Panel **e** is an Mn intensity map for a garnet grain from sample CPCS-2

absence of internal zonation (deep purple shading, Fig. 5d; outermost rim composition: $Alm_{73-80}Grs_{15-20}Prp_{5-10}Sps_{0-1}$). A tortuous boundary between the internal and external growth zones is consistent with some degree of resorption following growth of the internal zone; however, the boundary is marked by a sharp ($< 100 \mu m$) change in spessartine concentration implying short length scales of diffusive modification. Garnet in sample ASL13-17 has a similar compositional range to LPM 09-2 and also has at least two growth zones (Fig. 5b, c), comprising a bell-shaped Mn-rich internal zone (hot shading, lower panel Fig. 5c; core composition: $Alm_{55-65}Grs_{20-26}Prp_{24-27}Sps_{5-15}$) surrounded by a Mn-poor external zone (cold shading, lower panel Fig. 5c; rim composition: $Alm_{73-81}Grs_{14-16}Prp_{9-12}Sps_{0-2}$). The boundary between these growth zones is defined by a step-like discontinuity in $X_{sps}$ content that occurs over a length scale of $< 100 \mu m$. Garnet in sample CPCS-2 is spessartine-rich and occurs as small ($< 100 \mu m$ diameter), euhedral and inclusion-free porphyroblasts. Atoll-shaped Mn zonation defines core domains (core composition: $Alm_{8-12}Grs_{9-11}Prp_{1-4}Sps_{71-79}$) which are surrounded by narrow rim domains ($< 20 \mu m$; rim composition: $Alm_{15-19}Grs_{4-9}Prp_{3-6}Sps_{65-73}$) with little discernable internal zonation (Fig. 5e).

Sodic clinopyroxene is present in sample LPM 09-2 as matrix blasts after primary igneous clinopyroxene with an omphacitic composition ($\sim Jd_{25}Ag_{20}Di_{55}$). No discernable

core-to-rim chemical zonation was observed in EPMA analyses.

## Phengite Rb–Sr geochronology

Statistically valid isochrons were obtained for six of twelve samples initially analyzed (Fig. 6; Table 2); the remaining samples yielded low Rb–Sr ratios ($< 1$), unsuitable for age determination. Bedrock samples yield Rb–Sr whole rock-phengite isochron dates of $47.37 \pm 0.41$ (LPM 09-2; $n = 5$, MSWD $= 9$), $44.57 \pm 1.68$ (VCSC-1; $n = 4$, MSWD $= 1.2$), $35.76 \pm 0.54$ (CPCS-2; $n = 3$, MSWD $= 22$) and $30.45 \pm 0.45$ (ASL13-2B; $n = 6$, MSWD $= 0.48$). Clast samples yield whole rock-phengite isochron dates of $45.18 \pm 0.33$ (ASL13-17; $n = 4$, MSWD $= 4.8$) and $32.46 \pm 0.32$ (ASL13-21; $n = 4$, MSWD $= 11$). Results of two-point isochron calculations are presented in Table S1.

## PT modeling

A suite of *PTX* pseudosections were calculated to constrain prograde *PT* paths and peak *PT* conditions for two mafic samples (LPM 09-2 and ASL13-17) and one impure quartz

**Table 1** Major element compositions of rock-forming minerals in samples used for P–T modeling. Oxides are reported in weight %, cations in c.p.f.u. and end-members in molar proportions

| | LPM-09-2 | | | | | | ASL13-17 | | | | | CPCS-2 | | | | | |
|---|---|---|---|---|---|---|---|---|---|---|---|---|---|---|---|---|---|
| Mineral: | Grt | Grt | Amp | Amp | Ms | Cpx | Grt | Grt | Amp | Amp | Ms | Grt | Grt | Amp | Amp | Ms | Ep |
| Analysis | core 4/25 | rim 4/6 | core 20/3 | rim 20/19 | | | core 3/15 | rim 3/2 | core 3/16 | rim 3/30 | | core 3/14 | rim 3/5 | core 2/2 | rim 2/16 | | |
| $SiO_2$ | 36.72 | 35.38 | 56.66 | 47.34 | 54.65 | 54.17 | 36.97 | 36.97 | 60.15 | 53.70 | 54.78 | 36.98 | 36.76 | 59.58 | 57.72 | 52.38 | 37.59 |
| $TiO_2$ | 0.21 | 0.05 | 0.03 | 0.04 | 0.13 | 0.05 | 0.06 | 0.03 | 0.00 | 0.02 | 0.07 | 0.10 | 0.04 | 0.02 | 0.00 | 0.04 | 0.06 |
| $Al_2O_3$ | 20.77 | 21.28 | 6.87 | 6.98 | 22.57 | 5.16 | 21.09 | 21.28 | 10.28 | 6.52 | 27.73 | 19.92 | 20.51 | 8.54 | 5.67 | 23.13 | 22.14 |
| $Cr_2O_3$ | 0.00 | 0.00 | 0.00 | 0.01 | 0.01 | 0.00 | 0.00 | 0.00 | 0.00 | 0.00 | 0.00 | 0.00 | 0.04 | 0.02 | 0.00 | 0.06 | 0.03 |
| $Fe_2O_3$ | 1.28 | 5.39 | 6.15 | 4.33 | 0.87 | 6.14 | 1.83 | 2.71 | 2.39 | 5.19 | 0.00 | 0.00 | 0.00 | 5.44 | 9.57 | 2.69 | 14.77 |
| FeO | 24.08 | 30.27 | 11.83 | 18.96 | 4.64 | 6.55 | 27.59 | 32.47 | 8.04 | 17.63 | 2.52 | 4.35 | 7.69 | 3.10 | 6.51 | 1.48 | 0.34 |
| MnO | 8.67 | 0.37 | 0.02 | 0.16 | 0.01 | 0.02 | 3.80 | 0.50 | 0.01 | 0.13 | 0.01 | 32.38 | 29.14 | 0.24 | 0.22 | 0.05 | 0.92 |
| MgO | 0.43 | 2.36 | 9.38 | 8.02 | 4.34 | 8.04 | 1.60 | 2.38 | 11.53 | 6.81 | 3.68 | 0.49 | 1.22 | 13.80 | 11.31 | 4.70 | 0.02 |
| CaO | 8.15 | 5.70 | 0.49 | 8.47 | 0.03 | 13.97 | 7.64 | 5.41 | 0.24 | 1.48 | 0.09 | 3.64 | 2.24 | 0.12 | 0.14 | 0.01 | 21.58 |
| $Na_2O$ | 0.00 | 0.03 | 6.77 | 2.85 | 0.06 | 5.61 | 0.02 | 0.01 | 6.95 | 6.26 | 0.31 | 0.04 | 0.04 | 7.22 | 7.14 | 0.07 | 0.00 |
| $K_2O$ | 0.01 | 0.01 | 0.01 | 0.24 | 11.14 | 0.00 | 0.03 | 0.01 | 0.04 | 0.08 | 8.75 | 0.01 | 0.08 | 0.00 | 0.02 | 10.20 | 0.03 |
| Total | 100.32 | 100.84 | 98.21 | 97.40 | 98.45 | 99.71 | 100.63 | 101.77 | 99.63 | 97.82 | 97.93 | 97.92 | 97.76 | 98.08 | 98.30 | 94.81 | 97.48 |
| Si | 2.96 | 2.83 | 7.97 | 7.17 | 3.58 | 2.00 | 2.95 | 2.93 | 8.04 | 7.84 | 3.50 | 3.06 | 3.04 | 8.02 | 8.01 | 3.52 | 3.02 |
| Ti | 0.01 | 0.00 | 0.00 | 0.01 | 0.01 | 0.00 | 0.00 | 0.00 | 0.00 | 0.00 | 0.00 | 0.01 | 0.00 | 0.00 | 0.00 | 0.00 | 0.00 |
| Al | 1.98 | 2.01 | 1.14 | 1.25 | 1.74 | 0.23 | 1.99 | 1.99 | 1.62 | 1.12 | 2.09 | 1.94 | 2.00 | 1.35 | 0.93 | 1.83 | 2.10 |
| Cr | 0.00 | 0.00 | 0.00 | 0.00 | 0.00 | 0.00 | 0.00 | 0.00 | 0.00 | 0.00 | 0.00 | 0.00 | 0.00 | 0.00 | 0.00 | 0.00 | 0.00 |
| $Fe^{3+}$ | 0.08 | 0.33 | 0.65 | 0.49 | 0.04 | 0.17 | 0.11 | 0.16 | 0.24 | 0.57 | 0.00 | 0.00 | 0.00 | 0.55 | 1.00 | 0.14 | 0.89 |
| $Fe^{2+}$ | 1.62 | 2.03 | 1.39 | 2.40 | 0.25 | 0.20 | 1.84 | 2.15 | 0.90 | 2.15 | 0.14 | 0.30 | 0.53 | 0.35 | 0.76 | 0.08 | 0.02 |
| Mn | 0.59 | 0.03 | 0.00 | 0.02 | 0.00 | 0.00 | 0.26 | 0.03 | 0.00 | 0.02 | 0.00 | 2.27 | 2.04 | 0.03 | 0.03 | 0.00 | 0.06 |
| Mg | 0.05 | 0.28 | 1.97 | 1.81 | 0.42 | 0.44 | 0.19 | 0.28 | 2.30 | 1.48 | 0.35 | 0.06 | 0.15 | 2.77 | 2.34 | 0.47 | 0.00 |
| Ca | 0.70 | 0.49 | 0.07 | 1.37 | 0.00 | 0.55 | 0.65 | 0.46 | 0.03 | 0.23 | 0.01 | 0.32 | 0.20 | 0.02 | 0.02 | 0.00 | 1.86 |
| Na | 0.00 | 0.01 | 1.85 | 0.84 | 0.01 | 0.40 | 0.00 | 0.00 | 1.80 | 1.77 | 0.04 | 0.01 | 0.01 | 1.88 | 1.92 | 0.01 | 0.00 |
| K | 0.00 | 0.00 | 0.00 | 0.05 | 0.93 | 0.00 | 0.00 | 0.00 | 0.01 | 0.01 | 0.71 | 0.00 | 0.01 | 0.00 | 0.00 | 0.88 | 0.00 |
| Cation | 8.00 | 8.00 | 15.00 | 15.00 | 6.99 | 4.00 | 8.00 | 8.00 | 14.94 | 15.21 | 6.83 | 7.97 | 7.97 | 14.97 | 14.99 | 6.93 | 7.98 |
| O | 12 | 12 | 23 | 23 | 11 | 6 | 12 | 12 | 23 | 23 | 11 | 12 | 12 | 23 | 23 | 11 | 13 |
| $X_{Fe}$ | 0.97 | 0.88 | 0.41 | 0.57 | 0.37 | 0.31 | 0.91 | 0.88 | 0.28 | 0.59 | 0.28 | 0.83 | 0.78 | 0.11 | 0.24 | 0.15 | 0.88 |
| Alm (Acm) | 54.66 | 71.80 | Gln | Hbl | | 17.91 | 62.59 | 73.52 | Gln | Fgln | | 10.19 | 18.20 | Gln | Mrbk | | |
| Grs (Di) | 23.70 | 17.32 | | | | 57.91 | 22.21 | 15.70 | | | | 10.93 | 6.79 | | | | |
| Prp (Jd) | 1.72 | 9.99 | | | | 24.19 | 6.47 | 9.61 | | | | 2.06 | 5.14 | | | | |
| Sps | 19.93 | 0.89 | | | | | 8.73 | 1.16 | | | | 76.81 | 69.86 | | | | |

$X_{Fe} = Fe^{2+}/(Fe^{2+} + Mg)$; mineral abbreviations after Whitney and Evans (2010)

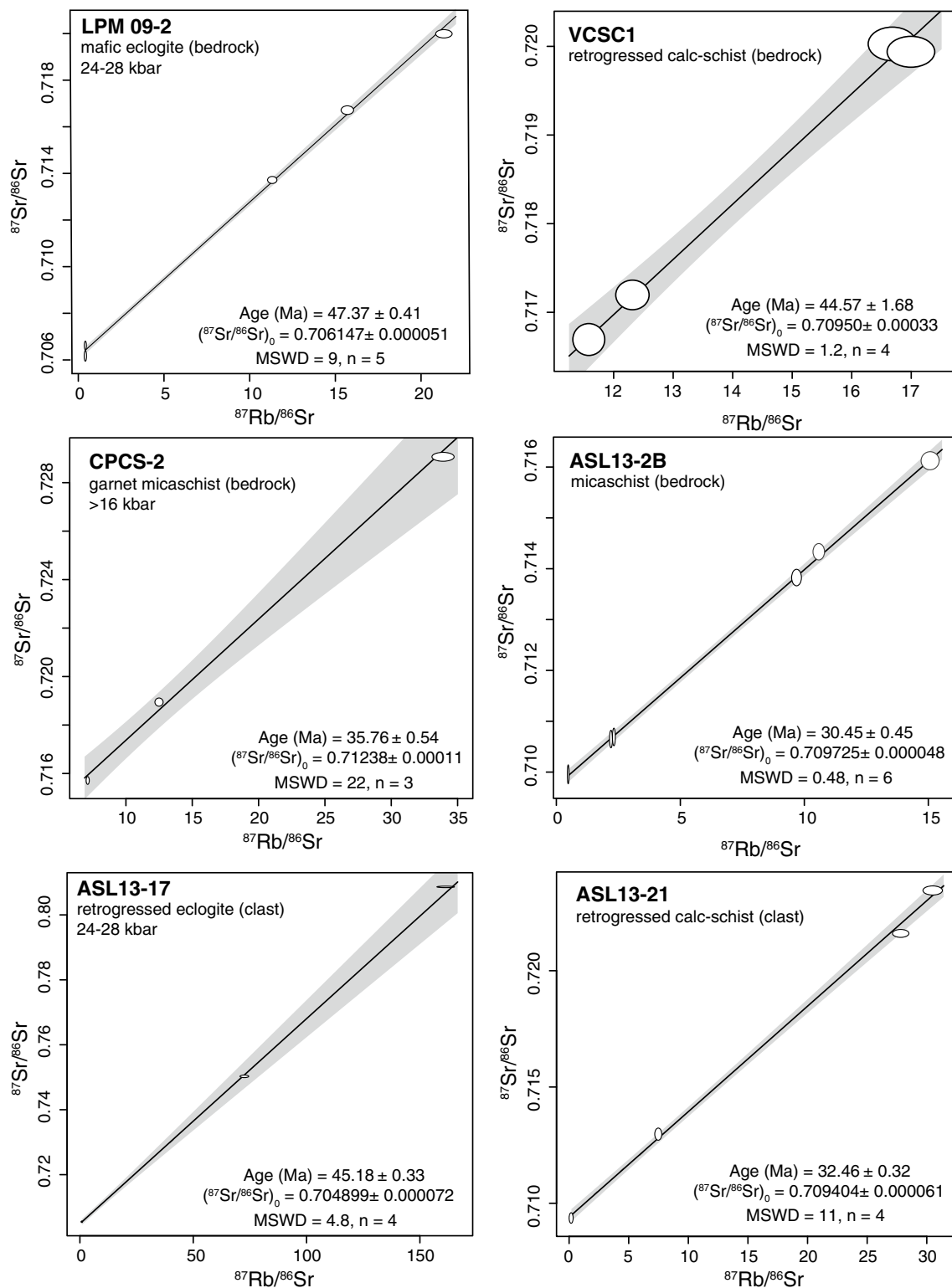$Fe^{3+}$ calculated assuming stoichiometric mineral compositions

**Fig. 6** White-mica Rb–Sr geochronology results

micaschist sample (CPCS-2). We focused on these samples due to their well-constrained Rb–Sr phengite ages and amenable phase assemblages to constrain the *PT* conditions of phengite equilibration. All calculations were performed in

the simplified (MnO–)$Na_2O$–CaO–$K_2O$–FeO–MgO–$Al_2O_3$–$SiO_2$–$H_2O$–$TiO_2$–$Fe_2O_3$ ((Mn–)NCKFMASHTO) chemical system using Gibbs free energy minimization as implemented in the Theriak-Domino program (de Capitani and

**Table 2** Rb–Sr white-mica geochronology

| Sample name | Lithology | Fraction | Rb [ppm] | Sr [ppm] | $^{87}Rb/^{86}Sr$ | $^{87}Sr/^{86}Sr$ |
|---|---|---|---|---|---|---|
| **Bedrock samples** | | | | | | |
| **LPM 09-2** (47.37 ± 0.41 Ma, $n$=5, MSWD=9, $^{87}Sr/^{86}Sr_i$=0.7061147±0.000051) | | | | | | |
| | Mafic eclogite | Wm (m=1.0A; 5.5 mg) | 324 | 38 | 21.4 | 0.71999 |
| | | Wm (m=1.0A; ~6.0 mg) | 364 | 58 | 15.7 | 0.71672 |
| | | Wm (m=1.0A; 49.9 mg) | 119 | 26 | 11.3 | 0.71372 |
| | | Whole rock (96.6 mg) | 20 | 130 | 0.377 | 0.70617 |
| | | Whole rock (239 mg) | 37 | 210 | 0.442 | 0.70662 |
| **ASL13-2B** (30.45 ± 0.45 Ma, $n$=6, MSWD=0.48, $^{87}Sr/^{86}Sr_i$=0.709725±0.000048) | | | | | | |
| | Quartz mica-schist | Wm (m=1.0A; ~8.0 mg) | 154 | 3 | 10.6 | 0.71433 |
| | | Wm (m=1.0A; ~8.0 mg) | 220 | 3 | 15.1 | 0.71611 |
| | | Wm (m=1.0A; 9.7 mg) | 508 | 12 | 9.74 | 0.71381 |
| | | Wm (m=1.0A; 5.7 mg) | 296 | 332 | 2.23 | 0.71065 |
| | | Wm (m=1.0A; 7.8 mg) | 294 | 325 | 2.26 | 0.71068 |
| | | Whole rock (3.8 mg) | 95 | 467 | 0.510 | 0.70996 |
| **VCSC-1** (44.57 ± 1.68 Ma, $n$=4, MSWD=1.2, $^{87}Sr/^{86}Sr_i$=0.70950±0.00033) | | | | | | |
| | Calc-schist | Wm (m=1.5A; 23.8 mg) | 376 | 55 | 17.0 | 0.71995 |
| | | Wm (m=1.5A; 12.1 mg) | 321 | 48 | 16.7 | 0.72003 |
| | | Whole rock (13.1 mg) | 89 | 19 | 11.6 | 0.71670 |
| | | Whole rock (10.6 mg) | 404 | 82 | 12.3 | 0.71719 |
| **CPCS-2** (35.76 ± 0.54 Ma, $n$=3, MSWD=22, $^{87}Sr/^{86}Sr_i$=0.71238±0.00011) | | | | | | |
| | Quartz mica-schist | Wm (m=0.5A; 19.8 mg) | 131 | 26 | 12.5 | 0.71897 |
| | | Wm (m=0.5A; 28.2 mg) | 126 | 9 | 34.0 | 0.72908 |
| | | Whole rock (21.4 mg) | 40 | 14 | 7.10 | 0.71573 |
| **Clast samples** | | | | | | |
| **ASL13-17** (45.18 ± 0.33 Ma, $n$=4, MSWD=4.8, $^{87}Sr/^{86}Sr_i$=0.704899±0.000072) | | | | | | |
| | Mafic blueschist | Wm (m=1.5A; ~1.2 mg) | 252 | 9 | 161.8 | 0.80861 |
| | | Wm (m=1.5A; 8.0 mg) | 33 | 1 | 64.1 | 0.74122 |
| | | Wm (m=1.5A; 5.4 mg) | 580 | 9 | 73.3 | 0.75044 |
| | | Whole rock (18.4 mg) | 17 | 41 | 1.035 | 0.70554 |
| **ASL13-21** (32.46 ± 0.32 Ma, $n$=4, MSWD=11, $^{87}Sr/^{86}Sr_i$=0.709404±0.000061) | | | | | | |
| | Calc-schist | Wm (m=1.0A; 12.4 mg) | 51 | 16 | 7.91 | 0.71322 |
| | | Wm (m=1.0A; 12.8 mg) | 42 | 4 | 27.8 | 0.72158 |
| | | Wm (m=1.0A; 12.9 mg) | 59 | 5 | 30.5 | 0.72345 |
| | | Whole rock (18.4 mg) | 5 | 58 | 0.210 | 0.70937 |

*2% Uncertainty applied to $^{87}Rb/^{86}Sr$ ratio and 0.01% uncertainty to applied to $^{87}Sr/^{86}Sr$ for isochron age calculation

Petrakakis 2010; version 11.03.2020). MnO was considered for the impure quartzite (CPCS-2) and for modeling the growth of garnet-core domains in the two mafic samples. All calculations were performed with $H_2O$ as a saturated component based on: (1) the presence of prograde pseudomorphs after lawsonite (sample LPM 09-2); (2) the prevalence of glaucophane in peak mineral assemblages; (3) the presence of idiomorphic white-mica aligned with peak-$P$ mineral fabrics samples, and (4) elevated XRF Loss On Ignition (LOI) values for samples LPM 09-2 and ASL13-17 (Table 3). It is likely, however, that some fraction of the LOI value reflects post-peak addition of $H_2O$ during exhumation.

All calculations were performed with the internally consistent thermodynamic database of Holland and Powell (1998; version ds5.5) and the following activity-composition ($a$–$X$) models: garnet, biotite (White et al. 2007), plagioclase (Holland and Powell 2003), chlorite, epidote, talc (Holland and Powell 1998), white mica (Coggon and Holland 2002), ilmenite (White et al. 2005), magnetite (White et al. 2002), clinoamphibole and clinopyroxene (Diener and Powell 2012). Quartz/coesite, aluminosilicate, albite, rutile, sphene, zoisite and lawsonite were all treated as pure phases; since we excluded $CO_2$ from consideration, the fluid phase was also treated as pure $H_2O$. The Holland and Powell (1998) ds5.5 thermodynamic database and derivative $a$–$X$ models were preferred over the more recent ds6.2 database (Holland and Powell 2011) for the following reasons: (1) calculations initially performed with the ds6.2 database and the updated amphibole and clinopyroxene models of Green et al (2016) yielded unreasonably high peak pressure estimates for garnet rim compositions (> 28 kbar), within the coesite stability field, for which there is no supporting petrographical evidence; (2) the consideration of $K_2O$ and $TiO_2$ components in Na and Na-Ca amphibole results in negligible differences in phase relations under the $PT$ conditions of interest, and (3) the ds5.5 database and models accurately predict the stability of lawsonite in garnet core assemblages and yield similar garnet compositions to those observed under non-UHP conditions.

Estimated bulk compositions were based on whole-rock XRF analyses for each of the samples (Table 3). Values of $XFe^{3+} = 0.30$ and $0.66$ ($XFe^{3+} = Fe^{3+}/(Fe^{3+} + Fe^{2+})$ in molar proportions) were assumed for the two mafic samples ($Fe_2O_3 = 2.11$, and 2 mol%, garnet core and rim compositions, sample LPM09-2; $Fe_2O_3 = 2.24$ and 1.73 mol%, sample LPM09-2) and the impure quartzite sample ($Fe_2O_3 = 1.3$ mol%, sample CPCS-2), respectively. These estimates were determined by comparison of ferric iron titration measurements—that tend to overestimate $XFe^{3+}$—and estimates of ferric iron concentrations derived by mineral modes and EPMA analyses. We note that a value of $XFe^{3+} = 0.3$ is agreeable with values reported for altered oceanic crust (e.g., $XFe^{3+} = 0.1 - 0.5$, Dungan et al. 1978) as well as for other massive Fe–Ti metagabbros from the Voltri massif (e.g., $XFe^{3+} = 0.21 - 0.37$, Starr et al. 2020).

Growth of porphyroblastic phases, such as garnet, at temperatures lower than required for grain-scale volume diffusion can modify the reactive bulk composition and subsequent prograde phase relations (e.g.,Evans 2004; Konrad-Schmolke et al. 2008; Marmo et al. 2002; Tinkham and Ghent 2005; Zeh 2006). To account for this in our calculations, we followed the approach presented by Evans et al. (2004) that applies a Rayleigh fractionation model based on the measured Mn content of garnet to derive the vectors of crystal fractionation. We applied this approach to samples LPM09-2 and ASL13-17 in which garnet is zoned in almandine, pyrope, grossular and spessartine components and is volumetrically abundant (> 10 vol%); garnet in sample CPCS-2 is present as a minor phase and any such fractionation is assumed to have had a negligible effect on the reactive bulk composition. For both samples, core-rim EPMA traverses were screened to identify the most primitive Mn-rich core compositions, reducing the risk of using an aliased, non-central chemical profile. Core-to-rim Mn transects exhibit classic bell-shaped zonation (Fig. 5), consistent with prograde formation during Rayleigh fractionation. Pseudosections for the formation of garnet cores were constructed using measured XRF bulk-rock compositions, whereas phase relations pertaining to equilibration of garnet rim domains were calculated using fractionated bulk compositions. All bulk compositions are presented in Table 3. Estimates of the $PT$ conditions of equilibration for garnet rims and cores were constrained by linearly-independent combinations of isopleths of almandine, pyrope, grossular and spessartine.

**Table 3** Bulk-rock XRF compositions used for pseudosection calculations (mole %)

| | LPM09-2 | | ASL13-17 | | CPCS-2 |
|---|---|---|---|---|---|
| | *Core* | *Rims* | *Core* | *Rims* | |
| **SiO₂** | 48.99 | 49.13 | 47.19 | 47.73 | 68.56 |
| **TiO₂** | 4.93 | 5.13 | 3.82 | 4.08 | 0.87 |
| **Al₂O₃** | 6.28 | 5.91 | 7.72 | 7.34 | 8.03 |
| **Fe₂O₃** | 2.11 | 2.00 | 2.24 | 1.73 | 1.30 |
| **FeO** | 9.63 | 9.31 | 10.29 | 8.23 | 1.33 |
| **MnO** | 0.25 | | 0.20 | | 1.45 |
| **MgO** | 9.61 | 9.96 | 9.59 | 10.05 | 4.69 |
| **CaO** | 6.43 | 6.23 | 5.48 | 5.32 | 3.14 |
| **Na₂O** | 4.25 | 4.42 | 3.71 | 3.96 | 0.68 |
| **K₂O** | 0.23 | 0.24 | 0.30 | 0.31 | 2.59 |
| **Total** | 92.71 | 92.33 | 90.54 | 88.75 | 92.64 |
| $^a XFe^{3+}$ | 0.30 | 0.30 | 0.30 | 0.30 | 0.66 |
| $^b LOI$ | 7.29 | 7.59 | 9.46 | 10.11 | 7.35 |

$^a XFe^{3+} = Fe^{3+}/(Fe^{3+} + Fe^{2+})$

$^b LOI =$ loss on ignition

## Sample LPM 09-2 (*bedrock mafic schist*)

The *PT* phase diagram calculated using the garnet core composition (Fig. 7a) is dominated by amphibole- and omphacite-bearing tri- and quadravariant assemblages. Garnet core compositions (composition used to constrain *PT* coordinates of isopleth intersection: $Alm_{54-55}Grs_{26-28}Sps_{19-21}$; Table 1) are calculated to be stable between 17–23 kbar and 460–510 °C in the phase assemblage field: grt-chl-omp-gln-lws-qz-(rt-ph-$H_2O$), in broad agreement with the presence of paragonite + clinozoisite pseudomorphs after lawsonite in garnet poikiloblasts (Fig. 5d). The ~ 5 kilobar pressure range obtained for garnet core growth reflects the poor level of fit between garnet isopleths. Conditions of outermost garnet rim equilibration (Fig. 7b; $Alm_{73-75}Grs_{14-16}Prp_{8-11}$; Table 1) are estimated to have occurred at higher pressures to core growth, around 24–25 kbar and 510–530 °C in the grt-omp-gln-tlc-qz-(rt-ph-lws-$H_2O$) assemblage field. This assemblage generally agrees with the observed mineral paragenesis with the notable exception that lawsonite is not preserved. It is plausible that lawsonite was indeed a constituent of the peak assemblage and underwent decomposition during retrograde, exhumation-related metamorphism. Support for this contention is provided by the presence of pseudomorphs in garnet rim domains of sample LPM09-2 (Fig. 5d). An alternative explanation is that the rock was undersaturated in $H_2O$ under peak metamorphic conditions and that the lawsonite stability field calculated assuming $H_2O$ saturation in Fig. 7b does not accurately reflect the metamorphic system. Fig. S1 displays *TX* phase relations for bulk compositions containing 2 to 20 mol percent $H_2O$ between 500 and 600 °C at 24.5 kbar. Inspection of the plot reveals that bulk-rock $H_2O$ concentrations of < 3 mol percent are required to stabilize lawsonite-absent equilibria and that under such $H_2O$-undersaturated conditions, garnet isopleths are strongly dependent on bulk-rock $H_2O$ and shift to lower-*T* with decreasing mole percent $H_2O$.

The observed range of Si-in-phengite (3.4–3.6 c.p.f.u..) corresponds to pressures < 23–24 kbar at peak temperatures of garnet rim equilibration (light blue lines, Fig. 7b), implying that phengite equilibrated during decompression from peak pressures.

## Sample ASL13-17 (*retrogressed eclogite clast*)

The topology of the garnet core *PT* pseudosection calculated for sample ASL13-17 is characterized by expansive tri- and pentavariant amphibole- and chlorite-bearing assemblages (Fig. 7c). Garnet core compositions (Fig. 7c; $Alm_{58-60}Grs_{24-26}Sps_{8-10}$; Table 1) correspond to a region of *PT* space between 17 and 19 kbar, and 480 and 510 °C spanning the low-P limit of clinopyroxene stability in the grt-omp-chl-ep-gln-lws-qz(-rt-ph-$H_2O$) assemblage field.

The garnet rim *PT* pseudosection (Fig. 7d) shares a similar topology to bedrock sample LPM09-2 (Fig. 7b), characterized by quadra- and pentavariant amphibole- and omphacite-bearing stability fields. Conditions of garnet rim equilibration are tightly constrained by measured garnet compositions ($Alm_{73-74}Grs_{14-16}Prp_{8-11}$; Table 1) to between 23–25 kbar and 515–530 °C, in the grt-omp-gln-lws-qz(-rt-ph-$H_2O$) assemblage stability field. The observed peak mineral assemblage (gln-ep-grt-ph-rt-qz) is notably devoid of clinopyroxene and lawsonite, both of which are predicted to be stable under peak *PT* conditions (~ 5 and ~ 15 vol.% omphacite and lawsonite, respectively, at 24 kbar and 525 °C). Epidote is predicted to be stable at pressures less than ~ 20 kbar, forming as a product of lawsonite and omphacite breakdown (e.g., Fig. 7d) and implying that the relict peak assemblage contained both of these phases and was similar to sample LPM09-2. Finally, the observed range of peak Si-in-phengite values (3.4–3.6 c.p.f.u.) occurs between ~ 20 and ~ 24 kbar at the peak temperature obtained from garnet rim isopleths, implying that phengite analyses with Si contents close to 3.6 c.p.f.u. preserve a record of peak-*P* conditions.

## Sample CPCS-2 (*bedrock metasediment*)

The *PT* pseudosection calculated for impure quartz-mica schist CPCS-2 is dominated by tri- and quadravariant garnet- and amphibole-bearing assemblages (Fig. 7e). Due to the Mn-rich bulk composition (MnO, 1.45 mol.%; Table 3), garnet stability is predicted to extend to low-grade conditions < 5 kbar and < 400 °C. Garnet core compositions ($Alm_{10-11,}$ $X_{Mg} = 0.17 – 0.18$; Table 1) correspond to *PT* conditions of 430–450 °C and 12–14 kbar, in the g-gl-chl-sph-ru-hem(-ep-ph-q-$H_2O$) stability field, whereas rim compositions ($Alm_{17-18}$, $X_{Mg} = 0.21 – 0.22$; Table 1) occur at higher pressures, between 18 and 19 kbar, at 450–470 °C, in the grt-gln-chl-rt-ilm(-ep-ph-qz-$H_2O$) stability field. The peak assemblage of grt-gln-rt-ep-ph-qz-$H_2O$ is in broad agreement with the predicted phase assemblage with the exception that chlorite was not identified in thin section. These peak *PT* conditions are in good agreement with observed Si-in-phengite values (3.4–3.6 c.p.f.u.), demonstrating that phengite with the highest Si contents equilibrated at pressures around 18–19 kbar; conversely, the lowest Si-content phengite corresponds to ~ 12 kbar at peak temperatures, similar to the pressures at which the observed replacement of rutile by sphene is predicted to occur.
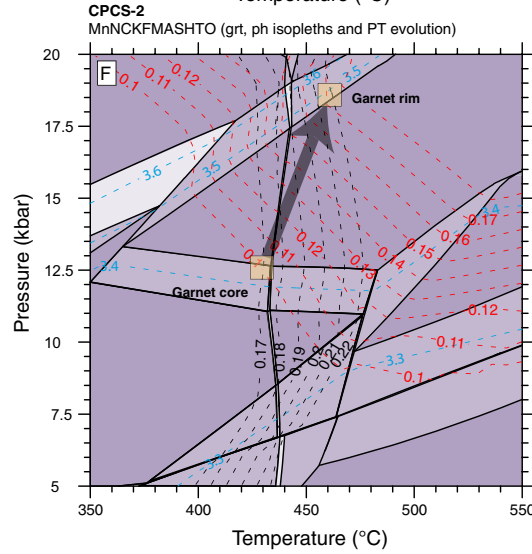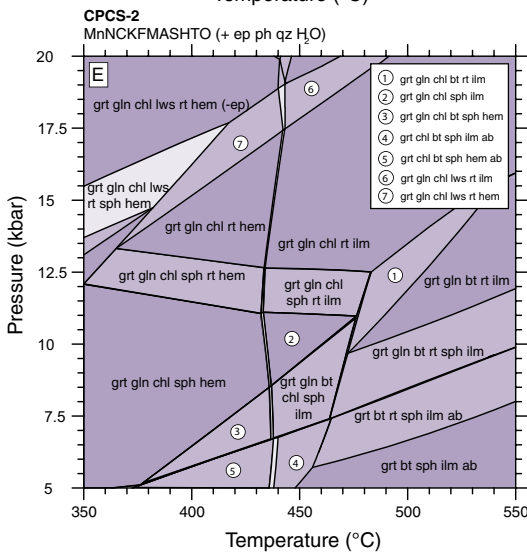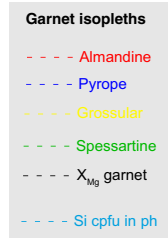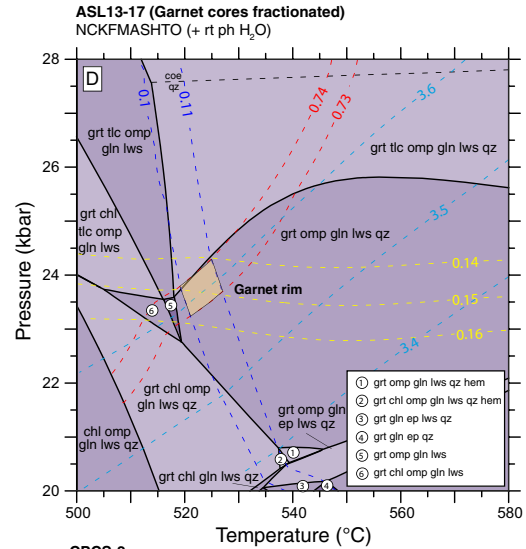
Figure panels A–F showing pseudosection phase diagrams of Pressure (kbar) versus Temperature (°C) for samples LPM09-2, ASL13-17, and CPCS-2. Garnet isopleth legend: Almandine (red dashed), Pyrope (black dashed), Grossular (yellow dashed), Spessartine (green dashed), X_Mg garnet (black dashed), Si cpfu in ph (light blue dashed).
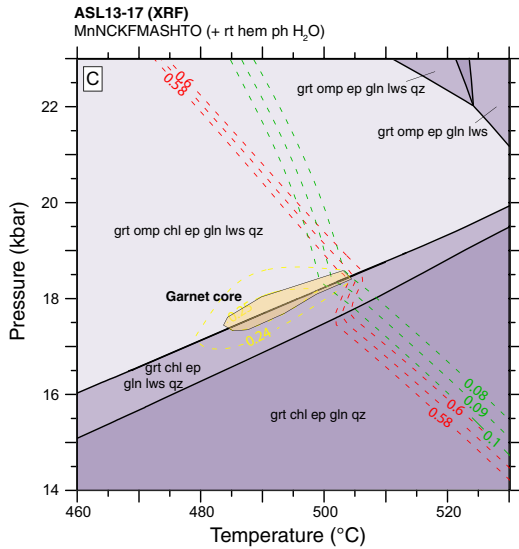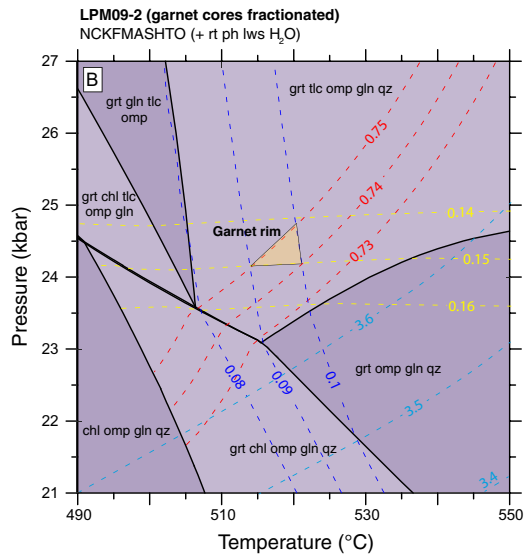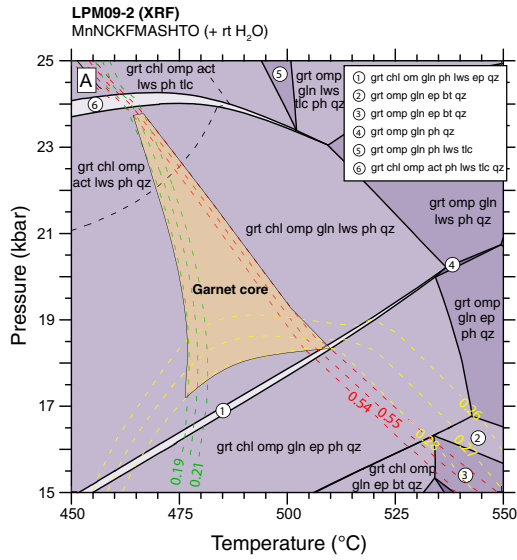
**Fig. 7** Phase equilibria modeling for samples LPM09-2 (panels **a**–**b**), ASL13-17 (**c**–**d**) and CPCS-2 (**e**–**f**). Pressure–temperature fields are shaded according to assemblage variance. Dashed lines correspond to observed ranges of garnet (mol fractions of almandine, pyrope, grossular and spessartine) and phengite (c.p.f.u. Si) compositions as determined by EPMA analyses. Beige polygons reflect best-fit conditions of garnet core and rim equilibration determined by intersection of isopleths. For samples LPM09-2 and ASL13-17 phase diagrams on the left (**a** and **c**) were calculated using bulk rock XRF compositions to model garnet core growth, whereas diagrams on the right (**b** and **d**) correspond to conditions of garnet rim growth. For sample CPCS-2 garnet core fractionation was not considered and panels **e** and **f** show phase relations and isopleths calculated using the bulk rock XRF composition, respectively. See text for discussion

## Interpretation of Rb–Sr white-mica dates

Combined, the *PT* modeling and Rb–Sr white-mica dates constrain segments of the prograde, peak and early-retrograde *PTt* paths for three samples. However, as four of the six samples analyzed here contain zoned phengite grains and the whole-grain Rb–Sr technique produces a volume-average of intracrystalline isotopic zonations, it is important to first consider the effect of intragranular chemical, and thus temporal, zonation on Rb–Sr isochron statistics.

Figure 8 shows a suite of isochrons calculated with synthetic Rb–Sr isotopic data that reflect different mixtures of high- and low-Si phengite ($X$ = volume fraction high-Si phengite). The data were generated assuming uniform distributions of equilibration ages between 45 and 50 Ma for phengite cores and 30–34 Ma for low-Si phengite overgrowths, as shown by $^{40}Ar$–$^{39}Ar$ data from Voltri white micas (Federico et al. 2005). The calculations also assume that $^{87}Rb/^{86}Sr$ varies between 10 and 40 for both mica generations and an initial $^{87}Sr/^{86}Sr$ value of 0.70970; these parameters were chosen to reflect the range in Rb–Sr isotopic compositions determined for the metasedimentary samples analyzed (VCSC1, CPCS-2, ASL13-2B, ASL13-21; Table 2), which exhibit evidence for low-Si phengite overgrowth on high-Si phengite cores.

Two principal conclusions can be drawn from the calculations. First, the computed isochron MSWD values exhibit a strong positive correlation with the volume fraction of low-Si phengite overgrowth, demonstrating that MSWD is potentially a useful indicator for the degree of isotopic heterogeneity in the analyzed mica population (e.g., Glodny et al. 2008; McIntyre et al. 1966; Wendt 1993). Second, for mixtures dominated by high-Si phengite (i.e., *X > 0.5*), isochron dates represent minimum estimates of the true age of high-Si phengite equilibration and conversely for mixtures dominated by low-Si phengite (*X < 0.5*), isochron dates represent maximum dates of the lower-*P* equilibration. Of course, these calculations are simplified and do not account for further complications associated with variations in $^{87}Sr/^{86}Sr_i$ between mica generations and progressive overgrowth of

low-Si phengite. Nevertheless, these principles provide a qualitative framework for the interpretation of the Voltri white-mica Rb–Sr. In addition to the complete multi-point Rb–Sr isochrons shown in Fig. 6, two-point isochrons connecting individual white-mica analyses with the whole rock fraction were calculated and are shown in Table S1. These two-point isochrons provide further constraints on the effect of mixing multiple mica generations on Rb–Sr isochron systematics and the timing of *HP* phengite growth.

White mica in the bedrock eclogite sample, LPM 09-2, is dominated by phengite and individual grains exhibit minor Si zonation, between 3.6 and 3.4 c.p.f.u., from core to rim domains. The pseudosection calculations (Fig. 7a, b) show that these phengite compositions correspond to a *P* difference of ~ 4 kbar recorded within individual mica grains, at temperatures corresponding to maximum metamorphic pressures (510–530 °C). Although the observed phengite Si contents are also calculated to be stable during a plausible prograde *PT* trajectory (Fig. 7b), the observation that phengite grains share straight grain boundaries with peak mineral phases, garnet, glaucophane and omphacite (Fig. 2a), supports the interpretation that phengite equilibrated close to peak *PT* conditions (24–25 kbar), likely during the initial stages of decompression at < 23 kbar. The elevated MSWD of the full Rb–Sr isochron (47.37 ± 0.41 Ma; MSWD = 9) and the presence of minor near-rim paragonite on some phengite grains implies that this date represents an estimate of the minimum age of *HP* metamorphism. Accordingly, we interpret the pair of two-point, whole rock-white mica, isochron dates that yield dates of ~ 48 ± 1 Ma as the best constraint on the age of *HP* phengite growth (Table S1).

White mica from the retrogressed eclogite clast ASL13-17 also exhibits minor variations in Si content, between 3.4 and 3.6 c.p.f.u., corresponding to an absolute *P* range of 4–5 kbar (Fig. 7d). Microtextural relations show that phengite equilibrated with chlorite during decompression-related consumption of garnet (Fig. 2e); this is consistent with phengite equilibration between ~ 20 and 24 kbar during the early stages of exhumation from peak *PT* conditions (23–25 kbar and 515–530 °C), notably similar to the interpretation proposed for bedrock mafic eclogite LPM09-2. The low MSWD (4.8) of the full Rb–Sr isochron (45.18 ± 0.33 Ma) supports the interpretation that this age is minimally impacted by retrograde white mica generations and represents the timing of *HP* phengite growth. We thus interpret that the sample underwent early decompression from peak conditions around ~ 45 Ma, consistent with the oldest two point isochron date of 45.86 ± 0.92 Ma (Table S1).

In contrast to the other metasediment samples investigated, phengite from micaschist CPCS-2 appears to preserve a restricted range in Si contents, between 3.4 and 3.6 c.p.f.u, overlapping the range of Si contents observed in phengite from the mafic samples. Phengite is present as a
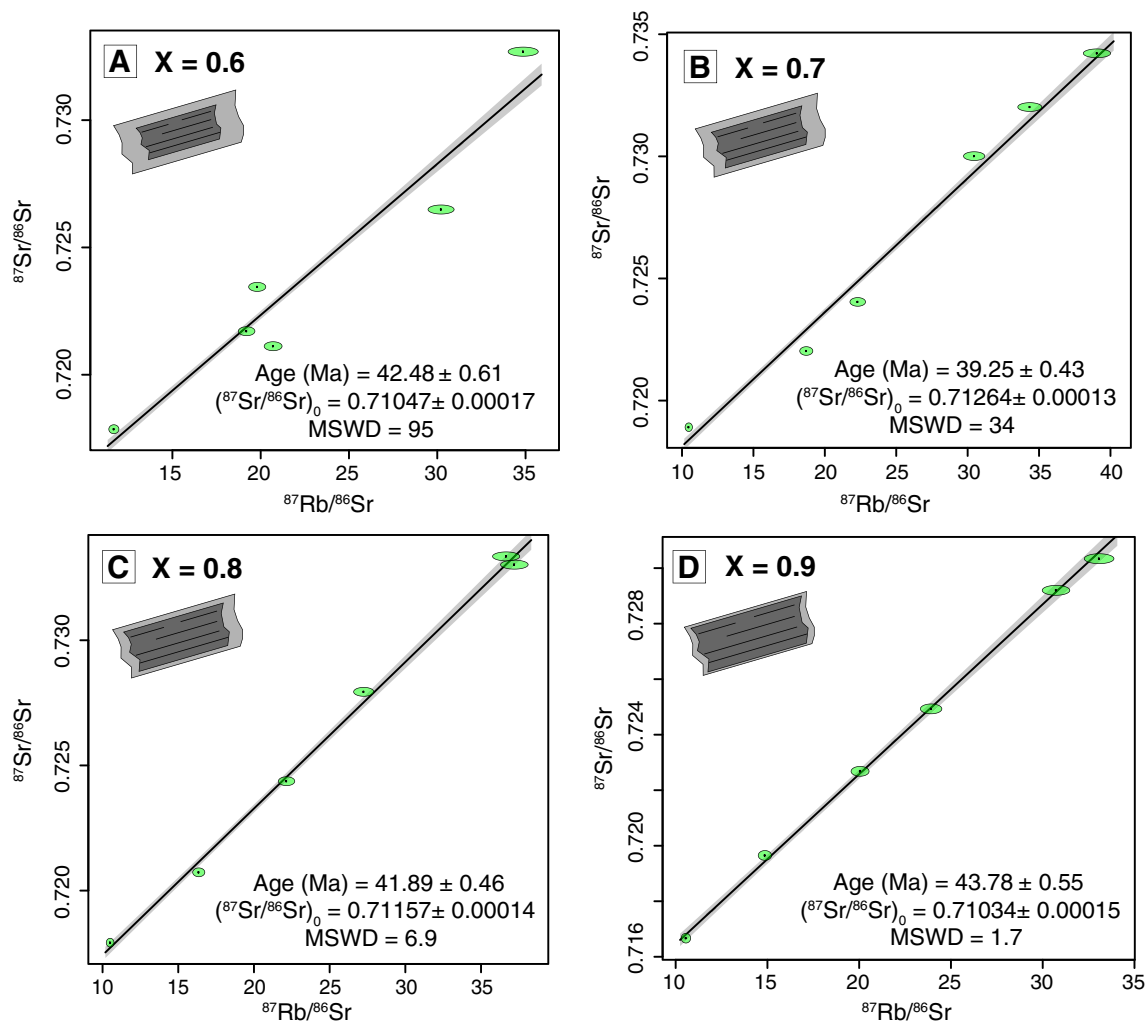
**Fig. 8** Effect of intragrain zonation on Rb–Sr isochron systematics. Panels **a–d** show synthetic data generated for different proportions ($X$ = vol. fraction phengite) of *HP* phengite (equilibration dates between 45 and 50 Ma, $^{87}Rb/^{86}Sr$ between 10 and 40, $^{87}Sr/^{86}Sr_i$ = 0.70970) and low-Si phengite overgrowth (equilibration dates between 30 and 34 Ma, $^{87}Rb/^{86}Sr$ between 10 and 40, $^{87}Sr/^{86}Sr_i$ = 0.70970). Nominal uncertainties of 1% and 0.01% ($1\sigma$) assumed for $^{87}Rb/^{86}Sr$ and $^{87}Sr/^{86}Sr$ ratios, respectively. Isochron statistics were computed using IsoplotR (Vermeesch 2018)

matrix phase and wraps porphyroblasts of garnet and Na-amphibole (Fig. 2d), implying that high-Si phengite was reoriented and underwent partial chemical equilibration (to Si 3.4 c.p.f.u.) during exhumation-related deformation. Pseudosection calculations show that the observed range in Si contents corresponds to a range of pressures between ~ 12 and 19 kbar at peak metamorphic temperatures of 450–470 °C. These *PT* conditions are in broad agreement with the wide range of peak *PT* conditions (~ 15–20 kbar and ~ 400–550 °C) reported by Federico et al (2007a, b) for mafic and metasedimentary blocks at the same locality. The elevated MSWD (22) of the Rb–Sr isochron for this sample is at odds with the limited range of phengite Si contents observed and implies that the phengite EPMA analysis did not fully characterize the diversity of phengite

chemistry present in the sample. Thus, we interpret that the full isochron age (35.76 ± 0.54 Ma) reflects the analysis of phengite fractions with significant retrograde components and we, therefore, consider the oldest two-point isochron date (42.93 ± 2.65 Ma, Table S1) as a minimum age constraint on the timing of phengite growth under retrograde blueschist facies conditions.

Quantitative *PT* constraints for the remaining three metasediments, ASL13-2B, ASL13-21 and VCSC1 were not derived due to their high variance mineral assemblages. However, each of these samples preserve relict high-Si phengite cores, overgrown to various extents by low-Si phengite rims (Fig. 3), and a broad positive correlation exists between Rb–Sr white mica date and the minimum mica Si-content observed (Fig. 9). This correlation, combined with the low

MSWD of each of the isochrons ($<11$), enables qualitative interpretations of the Rb–Sr phengite dates. The well-preserved high-Si phengite cores in sample VCSC1 (Fig. 3) are consistent with the interpretation that this sample records *HP* conditions at $44.57 \pm 1.68$ Ma. In contrast, samples ASL13-2B and ASL13-21 exhibit a greater volume fraction of phengite grains with a progressive spread in Si contents between ~ 3.6 and 3 c.p.f.u., indicating that the Rb–Sr isochrons are likely dominated by low-Si phengite and represent upper bounds to the timing of white mica equilibration during exhumation, between 30 and 33 Ma.

In summary, the analyzed samples constrain the timing of phengite equilibration under eclogite and blueschist facies conditions to between ~ 49 and ~ 40 Ma. This age range is derived from: (1) the upper bound to the two-point isochron date for sample LPM09-2 ($48 \pm 1$ Ma), and (2) the lower bound to the two-point isochron for sample CPCS-2 ($42.93 \pm 2.65$ Ma); excluding uncertainties reduces the range to ~ 48–43 Ma. Recrystallization of *HP* phengite to low-Si phengite occurred between ~ 33 and ~ 30 Ma. These dates overlap both the range of phengite $^{40}$Ar–$^{39}$Ar dates reported by Federico et al (2005), who obtained eclogite and blueschist facies phengite dates between 40 and 49 Ma, and a greenschist facies overprint between 32 and 34 Ma, and the Sm–Nd garnet dates from Starr et al (2020) who reported ages of ~ 40 Ma and ~ 50 Ma from the central and northwestern Voltri Unit, respectively.
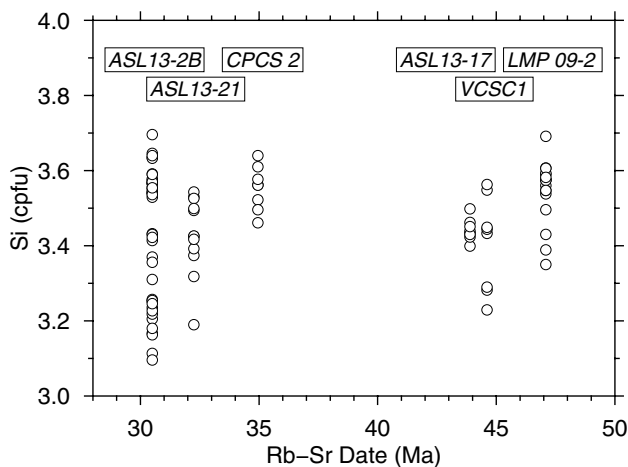


**Fig. 9** Relationship between white-mica Rb–Sr date and Si-content. Individual data points correspond to EPMA spot analyses

## Tectonic evolution of the Voltri Unit

### Diachronous *HP* metamorphism

Combined with existing datasets, the *PTt* data presented here allow for discrimination between competing structural models for the metamorphic evolution of the Voltri Unit. Contiguous *PTt* histories from across the unit would suggest that the Voltri Unit behaved as a single, coherent terrane during subduction and exhumation; rather, disparate and diachronous *PTt* histories would suggest an amalgamation of discrete subunits.

Following Starr et al (2020), a compilation of available geochronological data for the Voltri Unit is presented in Fig. 10. Inspection of the data shows a diachronous distribution of *HP* mineral dates across the Voltri Unit. Peak *HP* metamorphism is oldest in the northwest Voltri Unit, where eclogite facies conditions were attained ~ 50 Ma as evinced by similar Sm–Nd garnet (sample V18-S617C01, Starr et al (2020)) and high-Si phengite Rb–Sr dates (sample LPM-09-2, $47.37 \pm 0.41$ Ma, *this study*). Eclogitic and metasedimentary blocks from the Cascine Parasi mélange structure yield distinctly younger $^{40}$Ar–$^{39}$Ar and Rb–Sr phengite dates, between ~ 45 and 40 Ma (Federico et al., (2007a, b) and the oldest two-point isochron date, $42.93 \pm 2.65$ Ma, sample CPCS-2, *this study*). Together with the disparate range of exotic *HP-LT* blocks preserved in the mélange, these dates imply a different origin and/or tectonic evolution to the central and northwestern portions of the Voltri Unit. In contrast to the northwest Voltri Unit, Sm–Nd garnet dates from the central portion of the Voltri Unit (Vara region) indicate that peak conditions (23–25 kbar, 500–525 °C) were attained ~ 10–12 Myr later, between 41 and 38 Ma (Starr et al. 2020). These garnet dates indicate that the U–Pb baddeleyite age of $33.6 \pm 1$ Ma obtained from a Ti-clinohumite vein in the Vara region by Rubatto and Scambelluri (2003) most likely represents post-peak crystallization and not *HP* conditions as originally interpreted. Peak conditions in metasediments of the central and eastern portion of the Voltri Unit occurred between 47 and 44 Ma (sample VCSC-1, *this study*; sample FL34 of Federico et al (2005), estimated *PT* conditions of > 15–16 kbar and 400–500 °C), implying that such metasediments experienced a distinct *PTt* evolution relative to neighboring metagabbros in the Vara region of the central Voltri massif. In agreement with previous investigations (Federico et al. 2005, 2007b; Starr et al. 2020), these data collectively show that peak *HP* conditions, between ~ 18 and ~ 25 kbar (~ 60–90 km; $\rho = 2.9$ g/cc), were attained at different times across the Voltri Unit, between ~ 50 and ~ 38 Ma, consistent with previous interpretations that the Voltri Unit comprises a sequence of discrete lithotectonic units as opposed to a structurally coherent unit.

**Fig. 10** Geochronology of the Voltri Unit. Compilation of available geochronological data. Horizontal bars correspond to 2σ errors. Data sources: U–Pb titanite and zircon (Vignaroli et al. 2010); U–Pb baddeleyite (Rubatto and Scambelluri 2003); $^{40}Ar$–$^{39}Ar$ mica (Barbieri et al. 2003; Federico et al. 2005); Sm–Nd garnet, (Starr et al. 2020), and Rb–Sr white-mica, *this study*. Age of onset of TPB sedimentation from Turco et al (1994) and Gelati and Gnaccolini (1998)
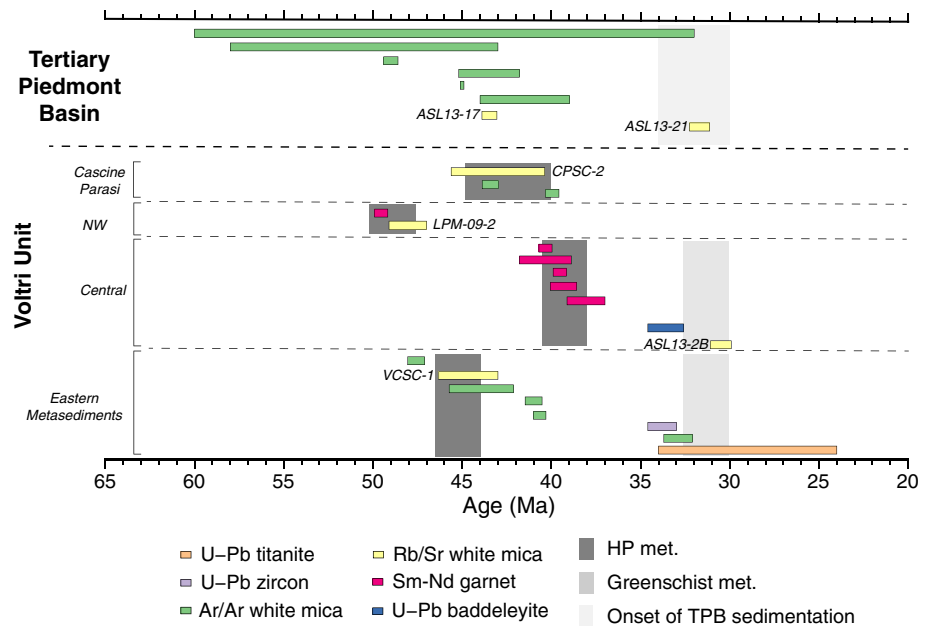


It is worth noting, however, that the current density of *PTt* sampling across the terrane precludes precise identification of the position and nature of the inferred tectonic boundaries that must separate the various sub-units.

Despite the ~ 12 Myr difference in age of *HP* metamorphism between the northwest and central Voltri Unit, the *PT* conditions of *HP* metamorphism define a restricted range of thermal gradients, between ~ 6 and ~ 8 °C/km ($\rho = 2.9$ g/cc). This observation implies that an active subduction regime was operating from the Early Eocene to the Eocene/Oligocene boundary.

The geochronological compilation also shows that the Rb–Sr white-mica dates presented here span a similar date range to $^{40}Ar$–$^{39}Ar$ white-mica dates reported previously for both clasts and bedrock samples that range from ~ 32 to ~ 65 Ma (Barbieri et al. 2003; Carrapa et al. 2003; Federico et al. 2005, 2007b). This similarity between datasets is expected if extraneous $^{40}Ar$ contamination is negligible. Furthermore, there is no systematic difference in the distribution of $^{40}Ar$–$^{39}Ar$ and Rb–Sr white mica dates for bedrock and clast samples, implying that the *HP* units of the Voltri Unit were juxtaposed prior to surface exposure and the timing of basal deposition in the adjacent TPB. The timing of basal sedimentation in the TPB (34–30 Ma) is also contemporaneous with several exhumation-related $^{40}Ar$–$^{39}Ar$ and Rb–Sr white mica dates (~ 30–33 Ma, samples ASL13-2B and ASL13-21, this study). This implies that (1) greenschist facies metamorphism was concomitant with erosion and sedimentation, and (2) at least the final stages of exhumation of *HP* units involved significant erosion at rapid rates.

## Exhumation of the Voltri Unit

Preservation of a protracted history of subduction in the Voltri Unit raises the question: *was exhumation continuous over this time interval?* As a precedent to the ensuing discussion, two end-member tectonic scenarios for the exhumation of the Voltri Unit are introduced: (1) exhumation occurred concurrently with subduction resulting in the continuous return of *HP* material to shallow crustal depths (e.g., Shreve and Cloos 1986), or (2) *HP* slices were accreted to the forearc under blueschist and eclogite facies conditions before abrupt exhumation and juxtaposition during the cessation of subduction (e.g., Bayet et al. 2018).

Using the conditions and timing of *HP* metamorphism and the onset of basal deposition in the TPB as constraints, time-averaged rates of exhumation are between 0.4 and 0.54 cm/year for the northwest Voltri Unit (calculated using durations of 16–20 Myr, *P* between 23 and 25 kbar and $\rho = 2.9$ g/cc) and between 0.73 and 1.74 cm/year in central Voltri Unit, respectively (durations of 5–11 Myr). In sufficient *PT* data are available to calculate exhumation rates for the eastern metasediments (e.g., sample VCSC-1). Such time-averaged rates are comparable to exhumation rates derived from other Alpine oceanic *HP* units, including the Schistes Lustres (e.g.,Agard et al. 2002) and the Gran Paradiso massif (e.g.,Manzotti et al. 2018). While affording a constraint on the total duration over which exhumation may have operated, these time-averaged exhumation rates do not account for: (1) potential storage of the tectonic slices that comprise the Voltri Unit during on-going subduction, and (2) the differential exhumation that must have occurred to facilitate tectonic juxtaposition prior to erosion as a coherent

package that explains the mixture of *HP* detritus preserved in the TPB.

In the northwestern sector of the Voltri Unit, garnet Sm–Nd and phengite Rb–Sr ages constrain peak pressure conditions to ~50 Ma (Starr et al. 2020), followed by phengite growth ~2–3 Myr later (*this study*; sample LPM 09–2, 49–47 Ma). This observation implies that exhumation initiated within 1–3 Myr of the attainment of peak eclogite-facies conditions, while subduction remained active. Assuming, (1) pressure differences between 1 and 4 kbar, and (2) a duration of between 1 and 3 Myr separate the conditions of garnet-rim and phengite equilibration results in rates of 0.12–1.40 cm/year ($\rho = 2.9$ g/cc) for this early stage of syn-subduction exhumation.

Several previous investigations have documented post-peak *HP* metamorphic overprints of the Voltri Unit that support the interpretation that a phase of *HP* exhumation occurred contemporaneous with active subduction. These include: (1) development of a post-eclogitic assemblage comprising Na-amphibole, phengite and garnet (Federico et al. 2005); (2) coexisting glaucophane and winchite idioblasts that cross-cut eclogite-facies foliations (Messiga and Scambelluri 1991), (3) formation of lower-pressure syn-tectonic blueschist facies assemblages (Vignaroli et al. 2005), and (4) reported retrograde blueschist-facies phengite growth at 8–15 kbar and 400–500 °C in eclogite clasts from the TPB at 45.2–41.8 Ma (Federico et al. 2005). Collectively, these constraints, when combined with the Rb–Sr phengite data, are consistent with the interpretation that individual sheets of *HP* material were detached from the downgoing plate, partially exhumed from peak pressures into the blueschist-facies (~8–20 kbar) and stored for durations between ~10 (central Voltri Unit) and ~15 Myr (northwest Voltri Unit) within the Alpine orogenic wedge. Final exhumation was likely facilitated by the cessation of subduction that accompanied arrival of the European continent into the subduction zone, ~32–34 Ma (e.g., Rubatto and Hermann 2001).

## Comparison with circum-Alpine *HP* units

The metamorphic history of the Voltri Unit shares common features with several of the circum-Alpine *HP* terranes. In particular, the Zermatt-Saas and Monviso ophiolites of the Western Alps represent coherent slices of Tethyan oceanic lithosphere that preserve a diachronous record of *HP* metamorphism that is remarkably similar to the Voltri Unit. In the Zermatt-Saas ophiolite, constraints on timing of eclogite-facies conditions span two ranges, the first between c. 52–46 Ma, interpreted to date prograde and peak metamorphism in the uppermost structural levels of the ophiolite, and the second, between 42 and 39 Ma, derived from samples in the Saas Fee and St. Jacques regions (Amato et al. 1999;

de Meyer et al. 2014; Lapen et al. 2003; Skora et al. 2015). In the case of the Monviso ophiolite, peak eclogite-facies conditions were attained between 51 and 45 Ma in the upper, Lago Superiore Unit, in contrast to the speculative ~40 Ma age proposed for the underlying Monviso unit (Angiboust and Glodny 2020; Duchêne et al. 1997; Garber et al. 2020; Rubatto and Angiboust 2015; Rubatto and Hermann 2003). The shared diachronous nature of these Alpine ophiolite units implies that they comprise an amalgamation of tectonic slices that underwent distinct *PTt* evolutions prior to juxtaposition.

Several of the circum-Alpine *HP* units also exhibit evidence for an initial phase of exhumation that occurred, while subduction was active. In the Eastern Alps, the Tauern Eclogite Zone underwent peak *HP* metamorphic conditions, 24–28 kbar, ~560 °C, at ~34 Ma (Glodny et al. 2005; Smye et al. 2011), followed by a retrograde epidote blueschist facies overprint at 400–450 °C, 10–15 kbar that occurred prior to collision and underplating of the leading edge of the European margin at ~30 Ma (e.g., Gleissner et al. 2007; Glodny et al. 2005). In the Western and Northwestern Alps, the Zermatt-Saas, Rocciavre and Monviso ophiolitic terranes also preserve evidence for overprinting of eclogite-facies peak assemblages under epidote blueschist conditions at 10–15 kbar and 400–450 °C (Angiboust et al. 2012; Schwartz et al. 2000); this retrograde event occurred between 39 and 35 Ma (Angiboust and Glodny 2020) contemporaneous with, or just preceding, deep subduction of the Internal Crystalline Massifs, such as the Dora Maira UHP continental slice (36–33 Ma) (e.g., Duchêne et al. 1997; Gebauer et al. 1997; Rubatto and Hermann 2001). This orogen-wide sequence of metamorphic events requires exhumation from depths of ~70–90 km to ~40–60 km, while subduction was active and before entry of continental basement into the Alpine subduction zone. As noted by Angiboust and Glodny (2020), this implies that additional forces, aside from the positive buoyancy force exerted by burial of continental crystalline material, are required to facilitate deep exhumation of the Alpine *HP* units.

## Implications for exhumation dynamics

Whereas shallow exhumation following continental collision can plausibly be driven by denudation of overburden (e.g., Platt 1993), the mechanisms responsible for deep exhumation during, or shortly after the cessation of active subduction are less certain. In the absence of return flow, two principal forces act on material along the subduction interface: shear stresses that operate along the interface and body forces resulting from the density contrast between slab-top and adjacent crustal or mantle rocks. Subduction occurs if shear forces exceed buoyancy forces. Constrained by

forearc heat-flow measurements, estimates of shear stresses at the maximum depth of thrust-faulting earthquakes along the plate-plate interface of modern subduction zones vary from ~ 20 to ~ 125 MPa (e.g., England 2018; Gao and Wang 2014). These estimates are consistent with the magnitudes of shear stress required to support topography above plate-plate interfaces (e.g., Davis et al. 1983; Lamb 2006; Suppe 2007). Along the plate-wedge interface estimates of the magnitude of shear stresses are typically < 20 MPa. These lower values of shear stress satisfy the requirement that the interface be strong enough to drive corner flow beneath the mantle wedge (Kelemen et al. 2003; McKenzie 1979) and paleo-piezometric estimates from exhumed *HP* rocks (e.g., Platt et al. 2018; Stöckhert et al. 1997).

Following England and Holland (1979), the magnitude of the buoyancy force ($h\Delta\rho gsin\theta$, where $h$ is interface width, $\Delta\rho$ is density contrast, $g$ is gravitational acceleration and $\theta$ is slab dip) relevant to typical slab-top materials is 1–5 MPa (assuming a slab dip of 20°, a density contrast of 300 kg/m$^3$ and an interface width of 1–3 km). Figure 11 shows the magnitude of the buoyancy force calculated for a wide range of parameters plotted against the estimates of interface shear stress described above. Shear stresses significantly exceed buoyancy forces along the plate-plate interface for reasonable values of interface width (< 10 km; Abers 2005), whereas along the plate-wedge interface, shear and buoyancy forces are of comparable magnitude (< 20 MPa). Given that the strengths of typical slab-top minerals, including antigorite (e.g., Hilairet et al. 2007), exceed the strength

of the interface required to facilitate subduction (< 2 MPa for interface widths of 1–5 km; England and Holland 1979), this simplified analysis indicates that: (1) exhumation by buoyancy forces alone during active subduction is unlikely along the plate-plate interface, and (2) that buoyancy-driven exhumation along the wedge-plate interface is plausible during subduction when shear stresses are < 10 MPa and channel widths are < 10 km.

Whether the Voltri *HP* rocks were exhumed from the wedge-plate interface is unclear, but inferences can be made from the fact that the maximum depth of thrust faulting earthquakes in active subduction zones is between 30 and 70 km (England 2018). Assuming that the maximum depth of thrust faulting earthquakes constrains the depth of the plate-plate-to-wedge-plate transition, it is plausible that some of the Voltri *HP* rocks were exhumed from the wedge-plate interface in response to low shear stresses.

The arguments developed in the preceding sections demonstrate that slab-top *HP* materials of the Voltri Unit were initially exhumed from > 70 km, potentially along the wedge-plate interface, then stored and refrigerated at depths of 30–70 km for > 10 Myr, while subduction was ongoing, before final exhumation on cessation of subduction. Several other studies provide supporting evidence for protracted forearc storage of *HP* rocks during active subduction. Bayet et al (2018) reported that a 4–5 km-thick package of clastic sediment, exposed in the southern Tianshan, underwent accretion and storage at ~ 80 km and ~ 540 °C for at least 2–5 million years. Eclogites from the Franciscan terrane preserve a record of ~ 7 Myr storage under blueschist facies conditions (Anczkiewicz et al. 2004; Mulcahy et al. 2009) and xenoliths from the Colorado Plateau yield zircon dates from 81 to 33 Ma, consistent with storage for ~ 50 Myr (Usui et al. 2003). Similar scenarios have also been proposed for protracted (> 40 Ma) storage of *HP* metamorphic rocks in Caribbean serpentinite mélanges (e.g., Blanco-Quintero et al. 2011; Krebs et al. 2008; Lázaro et al. 2009).
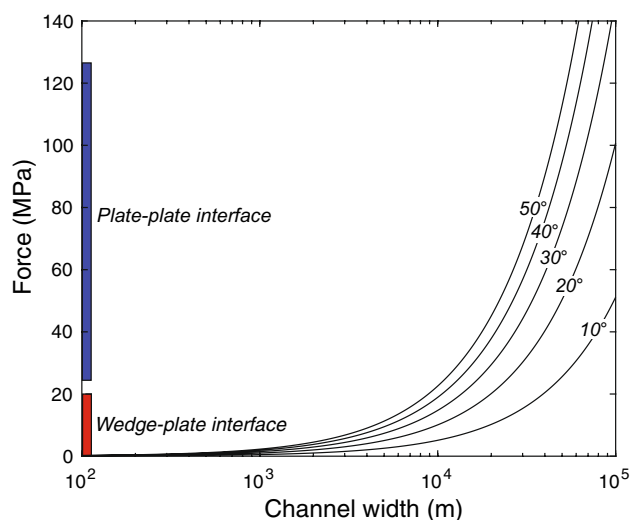


**Fig. 11** Force balance on the subduction interface. Plot shows the magnitude of buoyancy force ($h\Delta\rho gsin\theta$, where $h$ is interface width, $\Delta\rho$ is density contrast, $g$ is gravitational acceleration and $\theta$ is slab dip) for a range of channel widths and subduction angles and ($\Delta\rho$ = 300 kg/m$^3$). Superimposed on the *y*-axis are estimated ranges of shear stress along the plate-plate (blue) and wedge-plate (red) interfaces. See text for discussion

## Conclusions

1. Phengitic white-mica hosted in bedrock metasediments and metagabbros of the Voltri Unit and detrital clasts of the adjacent Tertiary Piedmont Basin is zoned in Si-content. Mineral core domains in phengite from six samples exceed Si 3.5 c.p.f.u., whereas rims are characterized by significantly lower values, Si < 3.3 c.p.f.u., implying that phengite grains partially re-equilibrated during decompression from *HP* conditions.

2. *PT* pseudosection calculations for bedrock and clast Fe–Ti metagabbros yield remarkably similar conditions for garnet-rim equilibration: 23–25 kbar and 510–530 °C. Phengite cores equilibrated during the early stages of

exhumation, ~ 20 and ~ 24 kbar. An impure quartzite bedrock sample preserves a record of lower-grade *HP* metamorphism with garnet-rim equilibration at 18–19 kbar and 450–470 °C. Core-to-rim celadonite contents in phengite corresponds to pressures between 19 and 12 kbar, respectively.

3. Interpreted as mixtures of high- and low-Si phengite, Rb–Sr phengite-whole-rock dates from the two eclogitic metagabbros constrain the timing of *HP* exhumation to between ~ 45 and ~ 50 Ma, marginally older than the age of *HP* phengite equilibration in the impure quartzite, $42.93 \pm 2.65$ Ma and a bedrock micaschist, $44.57 \pm 1.68$ Ma.

4. Exhumation-related recrystallization of *HP* phengite to low-Si phengite in two metasedimentary samples occurred between ~ 33 and ~ 30 Ma, contemporaneous with the onset of deposition in the TPB and consistent with previous $^{40}Ar-^{39}Ar$ constraints on the timing of greenschist metamorphism.

5. These *PTt* data collectively show that peak *HP* conditions, between ~ 18 and ~ 25 kbar were attained at different times across the Voltri Unit, between ~ 50 and ~ 40 Ma, consistent with the interpretation that the Voltri Unit comprises an assembly of discrete lithotectonic units that were juxtaposed prior to erosion and deposition in the TPB molasse basin.

6. Combined with existing garnet Sm–Nd and phengite $^{40}Ar-^{39}Ar$ mineral dates and reported metamorphic mineral textures, the Rb–Sr phengite *PTt* data reported here support a model in which individual sheets of *HP* material were detached from the downgoing plate, partially exhumed from peak pressures to 8–20 kbar, and stored for > 10 Myr within the Alpine orogenic wedge, until subduction ceased on arrival of the European continent into the subduction zone.

# References

Abers GA (2005) Seismic low-velocity layer at the top of subducting slabs: observations, predictions, and systematics. Phys Earth Planet Inter 149(1–2):7–29

Agard P, Monié P, Jolivet L, Goffé B (2002) Exhumation of the Schistes Lustrés complex: in situ laser probe 40Ar/39Ar constraints and implications for the Western Alps. J Metamorph Geol 20(6):599–618

Agard P, Yamato P, Jolivet L, Burov E (2009) Exhumation of oceanic blueschists and eclogites in subduction zones: timing and mechanisms. Earth Sci Rev 92(1–2):53–79

Agard P, Plunder A, Angiboust S, Bonnet G, Ruh J (2018) The subduction plate interface: Rock record and mechanical coupling (from long to short time scales). Lithos

Amato JM, Johnson CM, Baumgartner LP, Beard BL (1999) Rapid exhumation of the Zermatt-Saas ophiolite deduced from high-precision Sm-Nd and Rb-Sr geochronology. Earth Planet Sci Lett 171(3):425–438

Anczkiewicz R, Platt JP, Thirlwall MF, Wakabayashi J (2004) Franciscan subduction off to a slow start: evidence from high-precision Lu–Hf garnet ages on high grade-blocks. Earth Planet Sci Lett 225(1–2):147–161

Angiboust S, Glodny J (2020) Exhumation of eclogitic ophiolitic nappes in the W. Alps: New age data and implications for crustal wedge dynamics. Lithos 1:105374

Angiboust S, Langdon R, Agard P, Waters D, Chopin C (2012) Eclogitization of the Monviso ophiolite (W. Alps) and implications on subduction dynamics. J Metamorph Geol 30(1):37–61

Banno S, Shibakusa H, Enami M, Wang C-L, Ernst W (2000) Chemical fine structure of Franciscan jadeitic pyroxene from Ward Creek, Cazadero area. Calif Am Miner 85(11–12):1795–1798

Barbieri C, Carrapa B, Di Giulio A, Wijbrans J, Murrell GR (2003) Provenance of Oligocene synorogenic sediments of the Ligurian Alps (NW Italy): inferences on belt age and cooling history. Int J Earth Sci 92(5):758–778

Bayet L, John T, Agard P, Gao J, Li J-L (2018) Massive sediment accretion at~ 80 km depth along the subduction interface: evidence from the southern Chinese Tianshan. Geology 46(6):495–498

Blanco-Quintero IF, Rojas-Agramonte Y, García-Casco A, Kröner A, Mertz D, Lázaro C, Blanco-Moreno J, Renne P (2011) Timing of subduction and exhumation in a subduction channel: evidence from slab melts from La Corea Mélange (eastern Cuba). Lithos 127(1–2):86–100

Blow WH (1969) Late Middle Eocene to Recent planktonic foraminiferal biostratigraphy. In: Proceedings of the first international conference on planktonic microfossils. vol 1. EJ Brill Leiden. pp. 199–422

Boyd F, Mertzman S (1987) Composition and structure of the Kaapvaal lithosphere, southern Africa. In: Magmatic processes: physicochemical principles. vol 1. The Geochemical Society, pp 13–24

Brouwer FM, Vissers RL, Lamb WM (2002) Metamorphic history of eclogitic metagabbro blocks from a tectonic melange in the Voltri Massif, Ligurian Alps. Italy Ofioliti 27(1):1–16

Capponi G, Crispini L, Federico L, Malatesta C (2016) Geology of the Eastern Ligurian Alps: a review of the tectonic units. Ital J Geosci 135(1):157–169

Carrapa B, Wijbrans J, Bertotti G (2003) Episodic exhumation in the Western Alps. Geology 31(7):601–604

Cimmino F, Messiga B (1979) I calcescisti del Gruppo di Voltri (Liguria Occidentale): le variazioni composizionali delle miche bianche in rapporto alla evoluzione tettonico-metamorfica alpina. Ofioliti 4(3):269–294

Cloos M, Shreve RL (1988) Subduction-channel model of prism accretion, melange formation, sediment subduction, and subduction erosion at convergent plate margins: 1. Background and description. Pure Appl Geophys 128(3–4):455–500

Coggon R, Holland T (2002) Mixing properties of phengitic micas and revised garnet-phengite thermobarometers. J Metamorph Geol 20(7):683–696

Compston W, Chappell B, Arriens P, Vernon M (1969) On the feasibility of NBS 70a K-feldspar as a Rb-Sr age reference sample. Geochim Cosmochim Acta 33(6):753–757

Davis PB, Whitney DL (2006) Petrogenesis of lawsonite and epidote eclogite and blueschist, Sivrihisar Massif. Turkey J Metamorph Geol 24(9):823–849

Davis D, Suppe J, Dahlen F (1983) Mechanics of fold-and-thrust belts and accretionary wedges. J Geophys Res Solid Earth 88(B2):1153–1172

de Capitani C, Petrakakis K (2010) The computation of equilibrium assemblage diagrams with Theriak/Domino software. Am Miner 95(7):1006–1016

de Meyer CM, Baumgartner LP, Beard BL, Johnson CM (2014) Rb–Sr ages from phengite inclusions in garnets from high pressure rocks of the Swiss Western Alps. Earth Planet Sci Lett 395:205–216

Diener J, Powell R (2012) Revised activity–composition models for clinopyroxene and amphibole. J Metamorph Geol 30(2):131–142

Duchêne S, Blichert-Toft J, Luais B, Télouk P, Lardeaux J-M, Albarede F (1997) The Lu–Hf dating of garnets and the ages of the Alpine high-pressure metamorphism. Nature 387(6633):586–589

Dungan M, Rhodes J, Long P, Blanchard D, Brannon J, Rodgers K (1978) The petrology and geochemistry of basalts from Site 396, Legs 45 and 46 of the deep sea drilling project. Init Rep Deep Sea Drill Proj 46:89–113

England P (2018) On shear stresses, temperatures, and the maximum magnitudes of earthquakes at convergent plate boundaries. J Geophys Res Solid Earth 123(8):7165–7202

England P, Holland T (1979) Archimedes and the Tauern eclogites: the role of buoyancy in the preservation of exotic eclogite blocks. Earth Planet Sci Lett 44(2):287–294

Ernst W (1981) Petrogenesis of eclogites and peridotites from the Western and Ligurian Alps. Am Miner 66(5–6):443–472

Ernst W (1988) Tectonic history of subduction zones inferred from retrograde blueschist PT paths. Geology 16(12):1081–1084

Evans T (2004) A method for calculating effective bulk composition modification due to crystal fractionation in garnet-bearing schist: implications for isopleth thermobarometry. J Metamorph Geol 22(6):547–557

Federico L, Capponi G, Crispini L, Scambelluri M, Villa IM (2005) 39Ar/40Ar dating of high-pressure rocks from the Ligurian Alps: evidence for a continuous subduction–exhumation cycle. Earth Planet Sci Lett 240(3–4):668–680

Federico L, Crispini L, Scambelluri M, Capponi G (2007a) Different PT paths recorded in a tectonic mélange (Voltri Massif, NW Italy): implications for the exhumation of HP rocks. Geodin Acta 20(1–2):3–19

Federico L, Crispini L, Scambelluri M, Capponi G (2007b) Ophiolite mélange zone records exhumation in a fossil subduction channel. Geology 35(6):499–502

Gao X, Wang K (2014) Strength of stick-slip and creeping subduction megathrusts from heat flow observations. Science 345(6200):1038–1041

Garber JM, Smye AJ, Feineman M, Kylander-Clark ARC, Matthews S (2020) Decoupling of zircon U-Pb and trace-element systematics driven by U diffusion in eclogite-facies zircon (Monviso metaophiolite, W. Alps). Contrib Mineral Petrol 175:1–25

Gebauer D, Schertl H-P, Brix M, Schreyer W (1997) 35 Ma old ultrahigh-pressure metamorphism and evidence for very rapid exhumation in the Dora Maira Massif. Western Alps Lithos 41(1–3):5–24

Gelati R, Gnaccolini M (1982) Evoluzione tettonico-sedimentaria della zona limite tra Alpi ed Appennini tra l'inizio dell'Oligocene ed il Miocene medio. Memorie della Soc Geol Ital 24:183–191

Gelati R, Gnaccolini M, Petrizzo MR (1998) Synsedimentary tectonics and sedimentation in the Tertiary Piedmont Basin, northwestern Italy. Riv Ital Paleontol Stratigr 104(2):193–213

Gerya TV, Stöckhert B, Perchuk AL (2002) Exhumation of high-pressure metamorphic rocks in a subduction channel: a numerical simulation. Tectonics 21(6):6-1-6–19

Gleissner P, Glodny J, Franz G (2007) Rb-Sr isotopic dating of pseudomorphs after lawsonite in metabasalts from the Glockner nappe, Tauern Window. Eastern Alps Eur J Mineral 19(5):723–734

Glodny J, Ring U, Kühn A, Gleissner P, Franz G (2005) Crystallization and very rapid exhumation of the youngest Alpine eclogites (Tauern Window, Eastern Alps) from Rb/Sr mineral assemblage analysis. Contrib Miner Petrol 149(6):699–712

Glodny J, Kühn A, Austrheim H (2008) Diffusion versus recrystallization processes in Rb–Sr geochronology: isotopic relics in eclogite facies rocks, Western Gneiss Region. Norway Geochimica et Cosmochimica Acta 72(2):506–525

Green E, White R, Diener J, Powell R, Holland T, Palin R (2016) Activity–composition relations for the calculation of partial melting equilibria in metabasic rocks. J Metamorph Geol 34(9):845–869

Hermann J, Müntener O, Scambelluri M (2000) The importance of serpentinite mylonites for subduction and exhumation of oceanic crust. Tectonophysics 327(3–4):225–238

Hilairet N, Reynard B, Wang Y, Daniel I, Merkel S, Nishiyama N, Petitgirard S (2007) High-pressure creep of serpentine, interseismic deformation, and initiation of subduction. Science 318(5858):1910–1913

Holland T, Powell R (1998) An internally consistent thermodynamic data set for phases of petrological interest. J Metamorph Geol 16(3):309–343

Holland T, Powell R (2003) Activity–composition relations for phases in petrological calculations: an asymmetric multicomponent formulation. Contrib Miner Petrol 145(4):492–501

Holland T, Powell R (2011) An improved and extended internally consistent thermodynamic dataset for phases of petrological interest, involving a new equation of state for solids. J Metamorph Geol 29(3):333–383

Jolivet L, Faccenna C, Goffé B, Burov E, Agard P (2003) Subduction tectonics and exhumation of high-pressure metamorphic rocks in the Mediterranean orogens. Am J Sci 303(5):353–409

Kelemen PB, Rilling JL, Parmentier E, Mehl L, Hacker BR (2003) Thermal structure due to solid-state flow in the mantle wedge beneath arcs. Geophys Monogr Am Geophys Union 138:293–311

Kimura G, Maruyama S, Isozaki Y, Terabayashi M (1996) Well-preserved underplating structure of the jadeitized Franciscan complex, Pacheco Pass. Calif Geol 24(1):75–78

Konrad-Schmolke M, O'Brien PJ, de Capitani C, Carswell DA (2008) Garnet growth at high-and ultra-high pressure conditions and the effect of element fractionation on mineral modes and composition. Lithos 103(3–4):309–332

Krebs M, Maresch W, Schertl H-P, Münker C, Baumann A, Draper G, Idleman B, Trapp E (2008) The dynamics of intra-oceanic subduction zones: a direct comparison between fossil petrological evidence (Rio San Juan Complex, Dominican Republic) and numerical simulation. Lithos 103(1–2):106–137

Lamb S (2006) Shear stresses on megathrusts: implications for mountain building behind subduction zones. J Geophys Res Solid Earth 111(B7):1

Lapen TJ, Johnson CM, Baumgartner LP, Mahlen NJ, Beard BL, Amato JM (2003) Burial rates during prograde metamorphism of an ultra-high-pressure terrane: an example from Lago di Cignana, Western Alps. Italy Earth Planet Sci Lett 215(1–2):57–72

Lázaro C, García-Casco A, Rojas Agramonte Y, Kröner A, Neubauer F, Iturralde-Vinent M (2009) Fifty-five-million-year history of oceanic subduction and exhumation at the northern edge of the Caribbean plate (Sierra del Convento mélange, Cuba). J Metamorph Geol 27(1):19–40

Leake BE (1978) Nomenclature of amphiboles. Am Miner 63(11–12):1023–1052

Liou J, Zhang R, Ernst W, Liu J, McLimans R (1998) Mineral paragen-eses in the Piampaludo eclogitic body, Gruppo di Voltri, western Ligurian Alps. Schweiz Miner Petrogr Mitt 78(2):317–335

Lorenz C (1969) Contribution a l'étude stratigraphique de l'Oligocène et du Miocène inférieur des confins liguro-piémontais. Atti Ist Geol Univ Genova 6(2):273–889

Manzotti P, Bosse V, Pitra P, Robyr M, Schiavi F, Ballevre M (2018) Exhumation rates in the Gran Paradiso Massif (Western Alps) constrained by in situ U-Th–Pb dating of accessory phases (mon-azite, allanite and xenotime). Contrib Miner Petrol 173(3):24

Marmo B, Clarke G, Powell R (2002) Fractionation of bulk rock com-position due to porphyroblast growth: effects on eclogite facies mineral equilibria, Pam Peninsula, New Caledonia. J Metamorph Geol 20(1):151–165

Maruyama S, Liou J (1988) Petrology of Franciscan metabasites along the jadeite-glaucophane type facies series, Cazadero. Calif J Pet-rol 29(1):1–37

McIntyre G, Brooks C, Compston W, Turek A (1966) The statistical assessment of Rb-Sr isochrons. J Geophys Res 71(22):5459–5468

McKenzie D (1979) Finite deformation during fluid flow. Geophys J Int 58(3):689–715

Messiga B (1987) Alpine metamorphic evolution of Ligurian Alps (North-West Italy): chemography and petrological constraints inferred from metamorphic climax assemblages. Contrib Miner Petrol 95(3):269–277

Messiga B, Scambelluri M (1991) Retrograde P-T-t path for the Voltri Massif eclogites (Ligurian Alps, Italy): Some tectonic implica-tions. J Metamorph Geol 9(1):93–109

Messiga B, Scambelluri M, Piccardo GB (1995) Chloritoid-bearing assemblages in mafic systems and eclogite-facies hydration of alpine Mg-Al metagabbros (Erro-Tobbio Unit, Ligurian Western Alps). Eur J Miner 1:1149–1168

Morten L, Brunfelt AO, Mottana A (1979) Rare earth abundances in superferrian eclogites from the Voltri Group (Pennidic Belt, Italy). Lithos 12(1):25–32

Mulcahy SR, King RL, Vervoort JD (2009) Lawsonite Lu-Hf geochro-nology: a new geochronometer for subduction zone processes. Geology 37(11):987–990

Nebel O, Mezger K (2006) Reassessment of the NBS SRM-607 K-feld-spar as a high precision Rb/Sr and Sr isotope reference. Chem Geol 233(3–4):337–345

Nebel O, Scherer EE, Mezger K (2011) Evaluation of the 87Rb decay constant by age comparison against the U-Pb system. Earth Planet Sci Lett 301(1–2):1–8

Platt J (1993) Exhumation of high-pressure rocks: a review of concepts and processes. Terra Nova 5(2):119–133

Platt JP, Xia H, Schmidt WL (2018) Rheology and stress in subduction zones around the aseismic/seismic transition. Prog Earth Planet Sci 5(1):24

Polino R, Dal Piaz G, Gosso G (1990) Tectonic erosion at the Adria Margin and accretionary processes for the Cretaceous orog-eny of the Alps. Mémoires de la Société géologique de France 156:345–367

Rieder M, Cavazzini G, D'yakonov YS, Frank-Kamenetskii VA, Got-tardi G, Guggenheim S, Koval PW, Mueller G, Neiva AM, Radoslovich EW (1998) Nomenclature of the micas. Clays Clay Miner 46(5):586–595

Romaniello S, Field M, Smith H, Gordon G, Kim M, Anbar A (2015) Fully automated chromatographic purification of Sr and Ca for isotopic analysis. J Anal At Spectrom 30(9):1906–1912

Rubatto D, Angiboust S (2015) Oxygen isotope record of oceanic and high-pressure metasomatism: a P-T–time–fluid path for the Mon-viso eclogites (Italy). Contrib Miner Petrol 170(5–6):44

Rubatto D, Hermann J (2001) Exhumation as fast as subduction? Geol-ogy 29(1):3–6

Rubatto D, Hermann J (2003) Zircon formation during fluid circula-tion in eclogites (Monviso, Western Alps): implications for Zr and Hf budget in subduction zones. Geochim Cosmochim Acta 67(12):2173–2187

Rubatto D, Scambelluri M (2003) U-Pb dating of magmatic zircon and metamorphic baddeleyite in the Ligurian eclogites (Voltri Massif, Western Alps). Contrib Mineral Petrol 146(3):341–355

Sánchez-Vizcaíno VL, Rubatto D, Gómez-Pugnaire MT, Trommsdorff V, Müntener O (2001) Middle Miocene high-pressure metamor-phism and fast exhumation of the Nevado-Filábride Complex. SE Spain Terra Nova 13(5):327–332

Scambelluri M, Strating EH, Piccardo G, Vissers R, Rampone E (1991) Alpine olivine-and titanian clinohumite-bearing assemblages in the Erro-Tobbio peridotite (Voltri Massif, NW Italy). J Meta-morph Geol 9(1):79–91

Scambelluri M, Müntener O, Hermann J, Piccardo GB, Trommsdorff V (1995) Subduction of water into the mantle: history of an Alpine peridotite. Geology 23(5):459–462

Scambelluri M, Bebout GE, Belmonte D, Gilio M, Campomenosi N, Collins N, Crispini L (2016) Carbonation of subduction-zone serpentinite (high-pressure ophicarbonate; Ligurian Western Alps) and implications for the deep carbon cycling. Earth Planet Sci Lett 441:155–166

Schmid SM, Fügenschuh B, Kissling E, Schuster R (2004) Tectonic map and overall architecture of the Alpine orogen. Eclogae Geol Helv 97(1):93–117

Schmid SM, Bernoulli D, Fügenschuh B, Matenco L, Schefer S, Schus-ter R, Tischler M, Ustaszewski K (2008) The Alpine-Carpathian-Dinaridic orogenic system: correlation and evolution of tectonic units. Swiss J Geosci 101(1):139–183

Schumacher JC (2007) Metamorphic amphiboles: composition and coexistence. Rev Miner Geochem 67(1):359–416

Schwartz S, Lardeaux J, Guillot S, Tricart P (2000) The diversity of eclogitic metamorphism in the Monviso ophiolitic complex, Western Alps. Italy Geodinamica Acta 13(2–3):169–188

Shemenda AI (1992) Horizontal lithosphere compression and subduc-tion: constraints provided by physical modeling. J Geophys Res Solid Earth 97(B7):11097–11116

Shreve RL, Cloos M (1986) Dynamics of sediment subduction, mel-ange formation, and prism accretion. J Geophys Res Solid Earth 91(B10):10229–10245

Skora S, Mahlen N, Johnson CM, Baumgartner LP, Lapen T, Beard BL, Szilvagyi E (2015) Evidence for protracted prograde meta-morphism followed by rapid exhumation of the Zermatt-Saas Fee ophiolite. J Metamorph Geol 33(7):711–734

Smye AJ, Bickle MJ, Holland TJ, Parrish RR, Condon DJ (2011) Rapid formation and exhumation of the youngest Alpine eclogites: a thermal conundrum to Barrovian metamorphism. Earth Planet Sci Lett 306(3–4):193–204

Starr PG, Broadwell KS, Dragovic B, Scambelluri M, Haws AA, Cad-dick MJ, Smye AJ, Baxter EF (2020) The subduction and exhu-mation history of the Voltri Ophiolite, Italy: evaluating exhuma-tion mechanisms for high-pressure metamorphic massifs. Lithos 376–377:105767

Stöckhert B, Massonne H-J, Nowlan EU (1997) Low differential stress during high-pressure metamorphism: the microstructural record of a metapelite from the Eclogite Zone, Tauern Window. Eastern Alps Lithos 41(1–3):103–118

Suppe J (2007) Absolute fault and crustal strength from wedge tapers. Geology 35(12):1127–1130

Tinkham DK, Ghent ED (2005) Estimating PT conditions of garnet growth with isochemical phase-diagram sections and the problem of effective bulk-composition. Can Miner 43(1):35–50

Turco E, Duranti D, Iaccarino S, Villa G (1994) Relationships between foraminiferal biofacies and lithofacies in the Oligocene Molare Formation and Rigoroso Marl: preliminary results from the Piota

River section (Tertiary Piedmont Basin, NW Italy). Giorn Geol 56(2):101–117

Usui T, Nakamura E, Kobayashi K, Maruyama S, Helmstaedt H (2003) Fate of the subducted Farallon plate inferred from eclogite xenoliths in the Colorado Plateau. Geology 31(7):589–592

Vanossi M, Corte Sogno L, Galbiati B, Messiga B, Piccardo G (1984) Geologia delle Alpi Liguri: dati, problemi, ipotesi. Memorie della Società Geologica Italiana 28:5–75

Vermeesch P (2018) IsoplotR: a free and open toolbox for geochronology. Geosci Front 9(5):1479–1493

Vignaroli G, Rossetti F, Bouybaouene M, Massonne HJ, Theye T, Faccenna C, Funiciello R (2005) A counter-clockwise P-T path for the Voltri Massif eclogites (Ligurian Alps, Italy). J Metamorph Geol 23(7):533–555

Vignaroli G, Rossetti F, Rubatto D, Theye T, Lisker F, Phillips D (2010) Pressure-temperature-deformation-time (P-T-d-t) exhumation history of the Voltri Massif HP complex, Ligurian Alps. Italy. Tectonics 29(6):1

Waight T, Baker J, Willigers B (2002) Rb isotope dilution analyses by MC-ICPMS using Zr to correct for mass fractionation: towards improved Rb–Sr geochronology? Chem Geol 186(1–2):99–116

Warren C, Waters D (2006) Oxidized eclogites and garnet-blueschists from Oman: P-T path modelling in the NCFMASHO system. J Metamorph Geol 24(9):783–802

Wendt I (1993) Isochron or mixing line? Chem Geol 104(1–4):301–305

Wessel P, Smith WH (1998) New, improved version of generic mapping tools released. Eos Trans Am Geophys Union 79(47):579–579

White R, Powell R, Clarke G (2002) The interpretation of reaction textures in Fe-rich metapelitic granulites of the Musgrave Block, central Australia: constraints from mineral equilibria calculations in the system K2O–FeO–MgO–Al2O3–SiO2–H2O–TiO2–Fe2O3. J Metamorph Geol 20(1):41–55

White R, Pomroy N, Powell R (2005) An in situ metatexite–diatexite transition in upper amphibolite facies rocks from Broken Hill. Aust J Metamorph Geol 23(7):579–602

White R, Powell R, Holland T (2007) Progress relating to calculation of partial melting equilibria for metapelites. J Metamorph Geol 25(5):511–527

Whitney DL, Evans BW (2010) Abbreviations for names of rock-forming minerals. Am Miner 95(1):185–187

Zeh A (2006) Calculation of garnet fractionation in metamorphic rocks, with application to a flat-top, Y-rich garnet population from the Ruhla Crystalline Complex, Central Germany. J Petrol 47(12):2335–2356